

3D-Printed Vascular Self-Healing Concrete

The Influence of Printing Direction on the Porosity and Flexural Strength of 3D-Printed Vascular Self-Healing Concrete

J. van der Wereld

3D-Printed Vascular Self-Healing Concrete

The Influence of Printing Direction on the
Porosity and Flexural Strength of 3D-Printed
Vascular Self-Healing Concrete

by

J. van der Wereld

Student Name	Student Number
Jimmy van der Wereld	5348080

Supervisors:

Dr. B. Šavija
T.R. van Woudenberg
Y. Xu
Z. Wan

Project Duration:

April 2023 - July 2023

Faculty:

Faculty of Civil Engineering and Geo-Sciences (CiTG), Delft

Cover:

3D-printed test piece (90° specimen)

Note:

The dot is used as a decimal separator



Preface

This report is the Civil Engineering Bachelor Thesis of Jimmy van der Wereld at TU Delft and is an addition to ongoing research on 3D-Printed Vascular Self-Healing Concrete. The research is done in Microlab and Stevin II at the faculty of Civil Engineering (CiTG), TU Delft.

Specialists interested in a model to estimate the air-void ratio of 3D-printed vascular concrete can find this in section 2.1, section 4.2, and Appendix A. Others interested in the influence of printing parameters on mechanical properties can find this in section 4.3.

Firstly, an acknowledgement goes out to Y. Xu and Z. Wan for daily supervising this project during its entire lifespan. Secondly, an acknowledgement goes out to Dr. B. Šavija and T.R. van Woudenberg for giving valuable advice and for attending the meetings. Lastly, an acknowledgement goes out to M. van Leeuwen and A. Thijssen for offering help while using the equipment during this research.

*Delft, June 2023
J. van der Wereld*

Summary

Concrete has a high chance of cracking during its service life, regardless of the quality of the concrete or the environment it is subject to. The cracking of concrete is highly unwanted since the reinforcement can rust, which will result in failure of the concrete cover and ultimately failure of the concrete element as a whole. To avoid the failure of concrete a self-healing vascular system can be implemented which seals the cracks with healing agents. This technique is moderately new, meaning research has to be done to understand and design the best possible vascular concrete.

This report answers the following research question: 'What is the influence of printing direction on the porosity and flexural strength of 3D-printed linear vascular concrete?', aiming to improve the understanding of the printing process's influence on concrete performance. The printing directions considered are: 0° , 45° , and 90° .

To test the influence of the printing direction a total of nine specimens have been made, two specimens of each printing direction (0° , 45° , and 90°), and three cast reference specimens. To test the porosity, each type of specimen has been CT scanned. A model is introduced to predict the porosity of 3D-printed vascular concrete. The flexural strength was tested with the three-point bending test after 28 days of curing.

The results show that the 45° printed specimen has the lowest porosity and highest flexural strength, however not enough specimens are made to validate this. The relatively high strength may be due to the interlocking of layers, which improves the isotropy of the specimen. The air void model predicts a porosity of 16.3% and 8.3% for the 0° and 90° printed specimens respectively, while the real air-void ratios were 1.27% and 1.28% respectively. The results also show an overall negative trend between porosity and flexural strength, which aligns with earlier research. It becomes clear that the printing direction significantly influences the porosity and flexural strength.

The results show that the 45° printed specimen is the most efficient design regarding porosity and strength, but more specimens have to be made to validate this.

Table of contents

Preface	i
Summary	ii
Nomenclature	vii
1 Introduction	1
2 Theory	2
2.1 Air void model	2
2.2 The 3D printer	4
2.2.1 3D printing	4
3 Methodology	5
3.1 Preparation of specimens	5
3.1.1 0° printing direction	6
3.1.2 45° printing direction	7
3.1.3 90° printing direction	8
3.2 CT scan	8
3.3 Three-point bending test	9
4 Results	10
4.1 CT scan	10
4.1.1 0° printed specimen	11
4.1.2 45° printed specimen	13
4.1.3 90° printed specimen	15
4.1.4 Reference specimen	17
4.1.5 Additional CT scanning results	18
4.2 Comparing results to the air void model	19
4.3 Three-point bending test	20
5 Discussion	22
6 Conclusions	23
7 Recommendations	24
References	25
A Background air void model	26
B Images of specimens	29
C Images of three-point bending test and cracked specimens	35

List of Figures

2.1	Representation of the air void model	2
2.2	(a) Visualisation of 3D printer principle (b) Image of 3D printer	4
3.1	Front view of a specimen being printed	5
3.2	Front view of 0 degrees printed specimen	6
3.3	Side view of 0 degrees printed specimen	6
3.4	Front view of 45 degrees printed specimen	7
3.5	Side view of 45 degrees printed specimen	7
3.6	Front view of 90 degrees printed specimen	8
3.7	Side view of 90 degrees printed specimen	8
3.8	Visualisation of three-point bending test of reference specimen	9
3.9	Visualisation of three-point bending test of 3D-printed specimen	9
4.1	The air-void ratio of each type of specimen	10
4.2	3D visualisation of pores in 0° printed specimen	11
4.3	Visualisation of the vascular system of the 0° printed specimen	11
4.4	Logarithmic histogram of pore distribution of 0° specimen	12
4.5	Visualisation of all pores in 0° specimen (volume > 0.004 mm ³)	12
4.6	(a) Transparent view of big pore (b) Solid view of big pore	12
4.7	3D visualisation of pores in 45° printed specimen	13
4.8	Visualisation of the vascular system of the 45° printed specimen	13
4.9	Logarithmic histogram of pore distribution of 45° specimen	14
4.10	Visualisation of all pores in 45° specimen (volume > 0.004 mm ³)	14
4.11	3D visualisation of pores in 90° printed specimen	15
4.12	Visualisation of the vascular system of the 90° printed specimen	15
4.13	Logarithmic histogram of pore distribution of 90° specimen	16
4.14	Visualisation of all pores in 90° specimen (volume > 0.004 mm ³)	16
4.15	3D visualisation of pores in reference specimen	17
4.16	Logarithmic histogram of pore distribution of reference specimen	17
4.17	Visualisation of all pores in reference specimen (volume > 0.004 mm ³)	18
4.18	Comparing the results of the CT scanning with the results of the model with (a) a graph plot and (b) a bar plot	19
4.19	(a) A bar graph showing the mean three point bending force of each type of specimen; (b) A plot showing the relation between the air-void ratio and the three point bending force	20
4.20	Flexural strength of every type of specimen	21
A.1	Determining the width of a side-bonded concrete line	27
A.2	Determining the height of a top-bonded concrete line	27
B.1	Front view of 0° specimen being printed	29
B.2	Top view of 0° specimen being printed	30
B.3	Image of finished 0° printed specimen	30
B.4	Front view of 45° specimen almost finished	31
B.5	Front view of vascular system being printed	32
B.6	Top view of 45° specimen being printed	32
B.7	front view of 90° specimen being printed	33
B.8	Top view of 90° specimen being printed	34
B.9	Front view of finished 90° specimen	34

C.1 (a) Front view of three-point bending test; (b) Back view of three-point bending test	35
C.2 Top view of both cracks in the 0° specimens	36
C.3 Side view of crack in the first 0° specimen	37
C.4 Side view of crack in the second 0° specimen	38
C.5 Top view of both cracks in the 45° specimens	39
C.6 Side view of crack in the first 45° specimen	40
C.7 Side view of crack in the second 45° specimen	41
C.8 Top view of both cracks in the 90° specimens	42
C.9 Side view of crack in the first 90° specimen	43
C.10 Side view of crack in the second 90° specimen	44
C.11 Top view of both cracks in the reference specimens	45
C.12 Side view of crack in the first Reference specimen	46
C.13 Side view of crack in the second Reference specimen	47
C.14 Side view of crack in the third Reference specimen	48

List of Tables

3.1	Printing parameters for each type of specimen	6
4.1	Results of CT scan	10
4.2	Additional results of CT scan	18
4.3	Input air void model	19
4.4	Three-point bending force	20
4.5	Cracking stress of specimens	21
6.1	Data of each type of specimen	23

Nomenclature

Abbreviations

Abbreviation	Definition
AM	Additive Manufacturing
CT	Computerized Tomography
LVDT	Linear Variable Differential Transformer
SP	SuperPlasticizer
VMA	Viscosity Modifying Admixture

Symbols

Symbol	Definition	Unit
A_0	Enclosed area	[mm ²]
$A_{0,ref}$	Enclosed area of reference specimen	[mm ²]
A_c	Area of concrete	[mm ²]
$A_{c,ref}$	Area of concrete of reference specimen	[mm ²]
A_{va}	Area of vascular system	[mm ²]
b_l	Width of concrete line	[mm]
b_t	Total width of specimen	[mm]
$b_{t,1}$	Total width of specimen when distance is known	[mm]
b_{va}	Width of vascular system	[mm]
d_h	Central horizontal distance between concrete lines	[mm]
d_v	Central vertical distance between concrete lines	[mm]
h_l	Height of concrete line	[mm]
h_t	Total height of specimen	[mm]
$h_{t,1}$	Total height of specimen when distance is known	[mm]
h_{va}	Height of vascular system	[mm]
I	Intensity	[W/m ²]
I_0	Initial Intensity	[W/m ²]
l_{va}	Length of vascular system	[mm]
n_h	Number of concrete lines in horizontal direction	[1,2,3...]
n_v	Number of concrete lines in vertical direction	[1,2,3...]
r_v	Air-void ratio	[‐]
$w_{b,h}$	Horizontal bonding	[mm]
$w_{b,v}$	Vertical bonding	[mm]
$\mu(s)$	Linear attenuation	[m ⁻¹]

Introduction

Concrete is subjected to all kinds of weather conditions, which is no problem if the concrete has enough concrete cover. The concrete cover can, however, be penetrated by water if the concrete cracks. This results in the exposure of the reinforcement to the environment. Concrete cracking is a process that is likely to occur regardless of the quality of the concrete mix, since reinforced concrete is designed to crack. After the cracks develop and the reinforcement is exposed to the environment, it is almost certain that the reinforcement will rust and deteriorate. Rusting steel has 2x higher unit volume than rust-free steel, which will result in failure of the concrete cover and ultimately failure of the concrete element (Cabrera, 1996).

Failure of concrete cover is highly undesirable, so the reinforcement's exposure to the environment should be avoided. This can be avoided by using 3D-printed vascular self-healing concrete (Wan et al., 2022). With this technique, a vascular system is embedded in the concrete that allows healing agents to flow through. This system can be realised by placing tubes or leaving out material. The system will crack together with the concrete and the healing agent will flow out of the vascular into the cracks to protect the reinforcement from further deterioration. One of the healing agents is epoxy resin, which acts as glue when it comes in contact with concrete. This vascular system is derived from several natural processes, such as the blood vessels which repair the skin whenever it is damaged, or the hollow tubes in the xylem of trees that transport water to the leaves (Li et al., 2020).

This new technique of vascular concrete sounds very promising for improving the durability and thus the lifespan of concrete elements. However, more research is needed to understand and design the best vascular concrete possible, since the presence of the vascular system and the printing direction (0° , 45° , and 90°) will influence the strength of the concrete specimen.

This report answers the following question: 'What is the influence of printing direction on the porosity and flexural strength of 3D-printed linear vascular concrete?'. Firstly, specimens will be prepared with different printing directions containing a 1D (linear) vascular system. During curing, a CT scan will be made of each type of specimen to analyse the microstructure. This data will be compared to the air void model. After 28 days of curing, a three-point bending test will be executed, testing the flexural strength of the specimens. This data can be related to the microstructure of the specimen. This report will only look at the flexural strength and porosity of concrete specimens containing a linear vascular system without reinforcement. This will be related to cast concrete. The concrete mix used for this research was already known from previous research by Y. Xu and Z. Wan.

This report is structured as follows. In chapter 2 the theory behind the different tests and air void model will be discussed. The methodology used to analyse the specimens is described in chapter 3. Moreover, the results will be discussed in chapter 4. Furthermore, chapter 5 will be interpreting the results. Additionally, chapter 6 will give a conclusion on the research question based on the results. Lastly, chapter 7 will discuss the limitations of the research and provide recommendations for future research.

2

Theory

This chapter will describe the theory behind a model that estimates the porosity and 3D printing to provide the necessary knowledge. Firstly, in section 2.1 a model will be introduced to estimate the air-void ratio of 3D-printed concrete. Furthermore, information about the printer and 3D printing is provided in section 2.2.

2.1. Air void model

The amount of air in concrete can significantly affect its mechanical properties. Constructing a model to estimate the number of air voids in 3D-printed concrete can therefore give an indication of the relative flexural strength of concrete specimens if the distribution is known. This model can then be used in making the most efficient design of 3D-printed concrete, having the lowest porosity. The model can be used by implementing printing parameters. The concrete lines have an elliptical shape with a certain height and width. The amount of air depends on the bonding, the contact between concrete lines, the greater the bonding, the lower the amount of air. The mathematical background of the model is described in Appendix A.

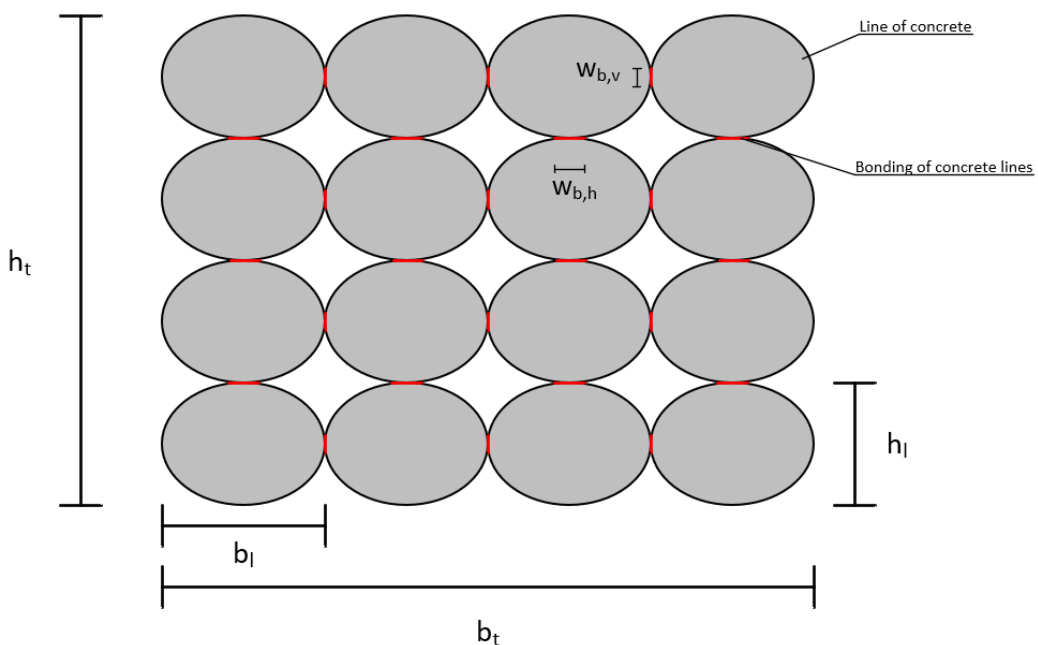


Figure 2.1: Representation of the air void model

The next assumptions are made in the model:

- The concrete lines are perfectly elliptical.
- The concrete specimen does not sag due to gravity.
- The concrete lines are constant, so there is no discontinuity or imperfection in the lines.

Firstly, the enclosed area can be determined with the following equation:

$$A_0 = b_t \cdot h_t \quad (2.1)$$

With:

- $b_t = \sqrt{\frac{b_l^2}{4} - \frac{w_{b,v}^2 \cdot b_l^2}{4 \cdot h_l^2}} \cdot (2n_h - 2) + b_l$; the total width of the specimen in [mm]
- $h_t = \sqrt{\frac{h_l^2}{4} - \frac{w_{b,h}^2 \cdot h_l^2}{4 \cdot b_l^2}} \cdot (2n_v - 2) + h_l$; the total height of the specimen in [mm]
- n_v, n_h : the total amount of concrete lines in vertical, and horizontal direction respectively
- b_l, h_l : the width and height of the concrete line respectively in [mm]
- $w_{b,v}, w_{b,h}$: the bonding width in vertical and horizontal direction respectively in [mm]

The area of concrete can be determined by the following formula:

$$A_c = n_v \cdot n_h \cdot \frac{1}{4}\pi \cdot b_l \cdot h_l \quad (2.2)$$

The air-void ratio can be determined by dividing the area of the voids by the area of the concrete. The area of the voids is calculated by subtracting the area of the vascular system (A_{va}) and the area of the concrete (A_c) from the enclosed area (A_0). Determining the area of the vascular system is described in Appendix A. The air-void ratio can be calculated with Equation 2.3.

$$r_v = \frac{A_0 - A_{va} - A_c}{A_0 - A_{va}} = 1 - \frac{n_v \cdot n_h \cdot \frac{1}{4}\pi \cdot b_l \cdot h_l}{b_t \cdot h_t - A_{va}} \quad (2.3)$$

The model does not take the porosity of the concrete itself into account. This is done by making use of a factor (α_m), which incorporates the porosity of the concrete itself. The value of α_m can be calculated according to Equation 2.4.

$$\alpha_m = \frac{A_{c,ref}}{A_{0,ref}} = 1 - r_{v,ref} \quad (2.4)$$

With the value of α_m known, it can be incorporated in Equation 2.3, this results in the following equation:

$$r_v = 1 - \alpha_m \cdot \frac{A_c}{A_0 - A_{va}} \quad (2.5)$$

One can also use this model and input the distance between concrete lines to get an estimate for the air-void ratio. This is done by substituting half the distance in the vertical and horizontal direction between the centre points of the lines in the equation for h_t and b_t respectively instead of the square root. The formula then becomes:

$$b_{t,1} = \frac{1}{2} \cdot d_h \cdot (2n_h - 2) + b_l \quad (2.6)$$

$$h_{t,1} = \frac{1}{2} \cdot d_v \cdot (2n_v - 2) + h_l \quad (2.7)$$

With d_h the horizontal centroidal distance between concrete lines and d_v the vertical centroidal distance between concrete lines. The values of $b_{t,1}$ and $h_{t,1}$ can then be substituted in Equation 2.1 for b_t and h_t and be further used for calculating the air-void ratio.

2.2. The 3D printer

The 3D printer is based on the extrusion of cementitious materials. The material is loaded into the cylinder and placed in the printer. After that, pressure will build up in the cylinder, pushing the material out through the tube and ultimately through the printing nozzle. The principle is shown in Figure 2.2a, while the printer itself is shown in Figure 2.2b.

The nozzle can move in x - and y -direction, while the platform the specimen is printed on can move in z -direction. While the nozzle extrudes material, the plunger lowers ensuring a constant pressure in the cylinder, lowering the chances of imperfections. The display on the right is used to control the machine and start printing.

2.2.1. 3D printing

Another commonly used term for 3D printing is additive manufacturing or additive layer manufacturing. It is the process of creating an object by dividing it into layers and building one layer at a time. The technique allows for greater product flexibility, lower production costs, and lower production time. The technique also allows for multiple materials to be used for production, which is quite hard to do with conventional manufacturing. The only downside of the technique is the cost of 3D printers and the overhang capability of the material. The overhang capability is a material property and has to do with the workability of the material. If the material has a low overhang capability, it will be hard to create flexible designs due to failure during the printing process (Linke, 2017).

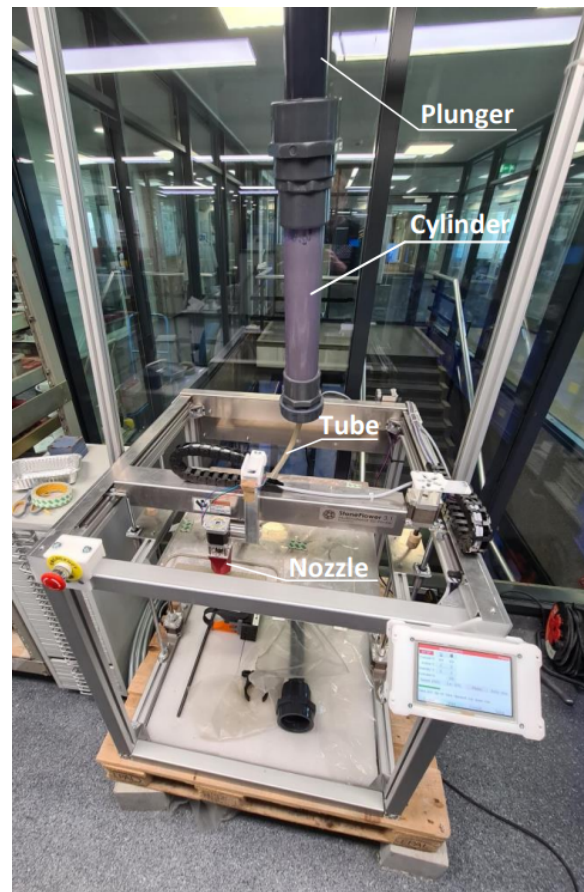
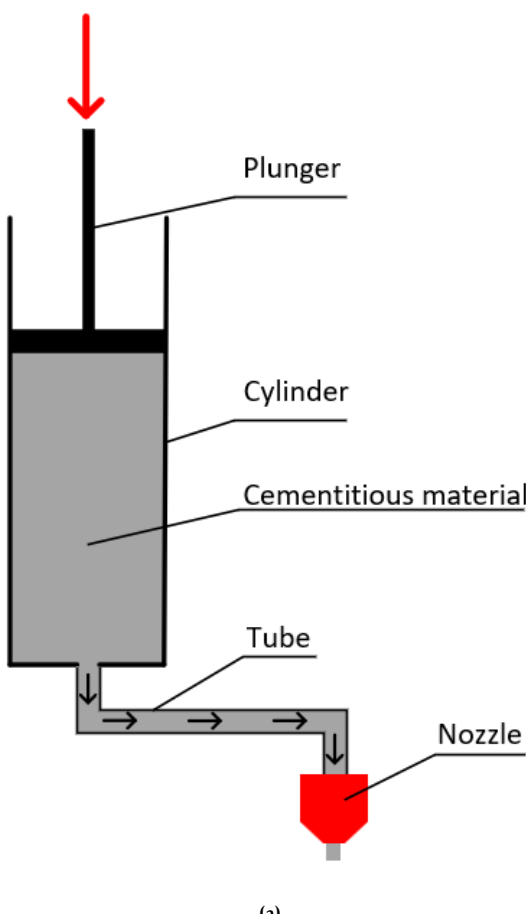


Figure 2.2: (a) Visualisation of 3D printer principle (b) Image of 3D printer

3

Methodology

This chapter describes the method that is used to obtain the results during this research. Firstly, the preparation of the specimens will be described in section 3.1. Furthermore, the CT scan will be explained in section 3.2. Lastly, the three-point bending test will be explained in section 3.3.

3.1. Preparation of specimens

The preparation of the specimen consists of a few steps. Firstly, the concrete mix needs to be made. An already-known mix was used for this experiment. The concrete mix consists of: (Note: the values are given as grams per 100 grams of concrete)

• CEMIII/B (cement):	69.964 [g/100g]
• Water:	23.975 [g/100g]
• Sand (0.125-0.250 mm):	5.910 [g/100g]
• Viscosity Modifying Admixture (VMA):	0.051 [g/100g]
• SuperPlasticizer (SP):	0.014 [g/100g]
• PolyEthylene fibres (PE):	0.085 [g/100g]

The preparation of the concrete mix is done as follows:

1. Add the cement, sand, and VMA to a mixing bowl and mix it either using a machine or by hand.
2. After four minutes of mixing, add the water with the SP and mix again for four minutes.
3. Now add the fibres and mix again for four minutes.

After the mixture is made, it can be loaded into the 3D printer. Figure 3.1 shows a specimen being printed. The line around the specimen is used by the printer to release any air in the printing nozzle and tube. More printing process images can be found in Appendix B. The information about the specimen is stored in Gcodes and loaded onto the 3D printer. After printing, the specimens will be transported to a curing room with a humidity of more than 95%.



Figure 3.1: Front view of a specimen being printed

The specimens all have different printing parameters, see Table 3.1. The table shows the concrete line width (b_l) and height (h_l), and the number of lines in horizontal (n_h) and vertical (n_v) direction of each type of specimen. Images of the printing process can be found in Appendix B.

Table 3.1: Printing parameters for each type of specimen

Printing direction	b_l [mm]	h_l [mm]	n_h	n_v
0°	5	3	41	13
45°	5	3	-	13
90°	5	3	11	13

The 3D-printed specimens have the following dimensions: 32.5 mm in height, 50 mm in width, and 200 mm in length, while the reference specimens are 40 mm in height, 40 mm in width, and 160 mm in length. The geometry of the reference specimen is a standard geometry, while the geometry for the printed specimens are existing designs from previous research. The 3D-printed specimen can be distinguished by printing direction.

3.1.1. 0° printing direction

The 0° printed specimens look like Figure 3.2 and Figure 3.3. All the layers in this specimen are printed in the 0° direction, as can be seen in the figures.

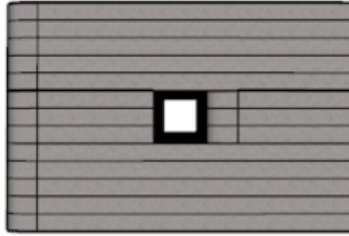


Figure 3.2: Front view of 0 degrees printed specimen

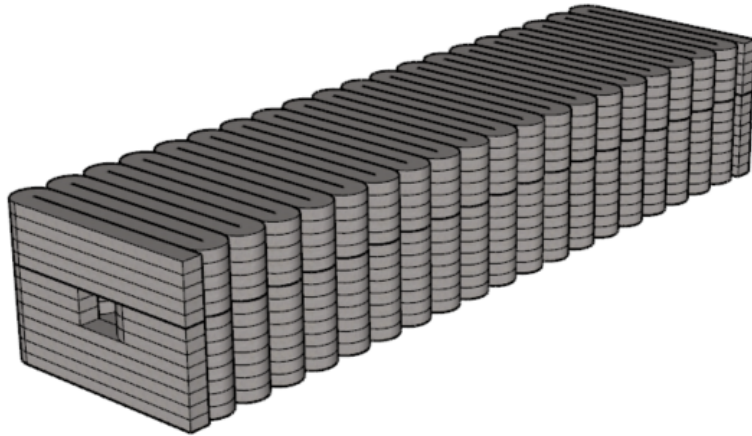


Figure 3.3: Side view of 0 degrees printed specimen

3.1.2. 45° printing direction

The 45° printed specimens look like Figure 3.4 and Figure 3.5. The first and last four layers of this specimen are 45° printed while changing direction every layer, this is done to make sure the material interlocks. The layer above the vascular system is 0° printed to ensure that the lines do not fall into the vascular system while printing. The layer below the vascular system is also 0° printed to make the specimen symmetrical.

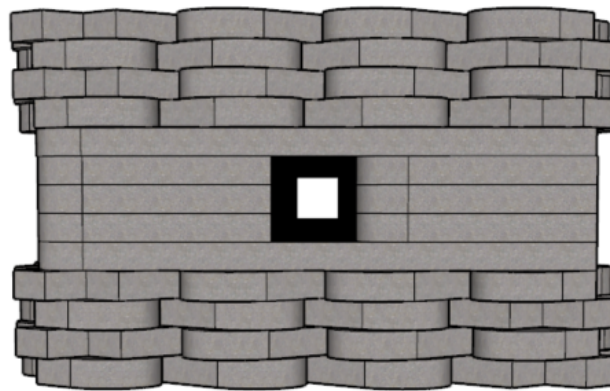


Figure 3.4: Front view of 45 degrees printed specimen

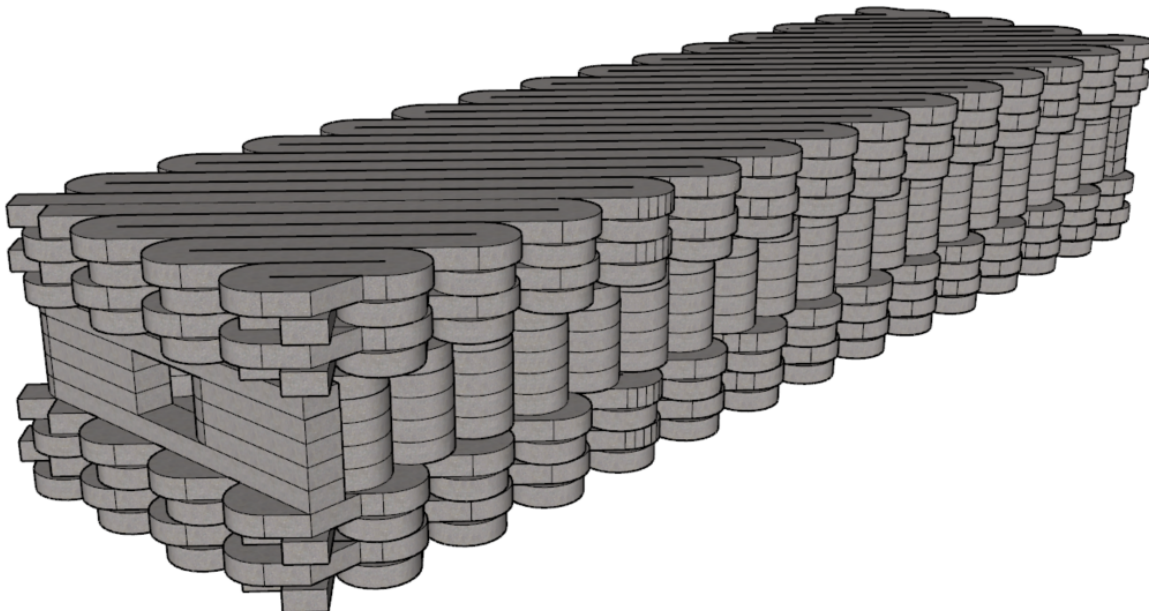


Figure 3.5: Side view of 45 degrees printed specimen

3.1.3. 90° printing direction

The 90° printed specimens look like Figure 3.6 and Figure 3.7. This specimen is very similar to the 45° specimen, but with this specimen, the first and last four layers are printed in the 90° direction.

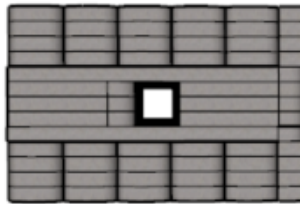


Figure 3.6: Front view of 90 degrees printed specimen

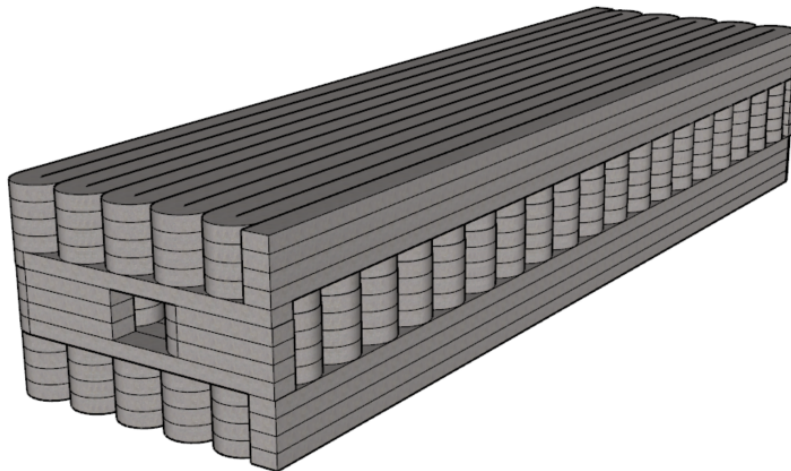


Figure 3.7: Side view of 90 degrees printed specimen

3.2. CT scan

After the specimens are finished, a CT scan is made of each type of specimen to analyse the microstructure. Investigating the microstructure of the specimens is useful in differentiating the flexural strength. This is done based on the porosity and number of imperfections in the specimen, which determines the printing quality. Before the specimen can be loaded up in the CT scanning machine, one side has to be cut to create a flat bottom for the specimen to stand on. The specimens will be scanned in five parts and will be reconstructed and analysed using the software Dragonfly. The CT scanning machine used in this research is the CoreTom from TESCAN (TESCAN, 2023). The following settings have been used while CT scanning:

- Tube voltage (set value): 140 [kV]
- Tube power (set value): 40 [W]
- Exposure time (set value): 200 [ms]
- Voxel size (set value): 40 [μm]

For this research a resolution of 40 μm was chosen, this is done in regard to the processability of the data. However, a higher resolution is more favourable to cover the smaller pores within the concrete. Because of this resolution, pores with a volume of at least 0.004 mm^3 are considered, and pores with a lower volume are considered as noise.

3.3. Three-point bending test

After the specimens are scanned using the CT scanning machine, a three-point bending test is executed to test the flexural strength of each type of specimen. The strength can be further used to analyse the differences between each specimen and relate it to the printing parameters. The machine used for the three-point bending test is a Servo Plus Evolution from Matest (Matest, 2023). The following setting has been used on the hydraulic press:

- Force increment speed: 0.1 [kN/s]

The setup and geometry of the three-point bending test for the reference and printed specimens are shown in Figure 3.8 and Figure 3.9. The three-point bending test will be executed based on force and will test the flexural strength of the specimens just before cracking occurs.

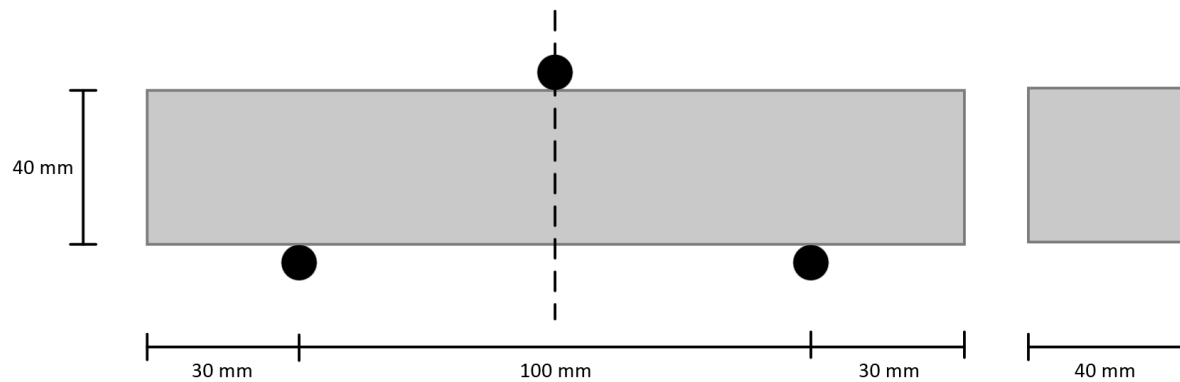


Figure 3.8: Visualisation of three-point bending test of reference specimen

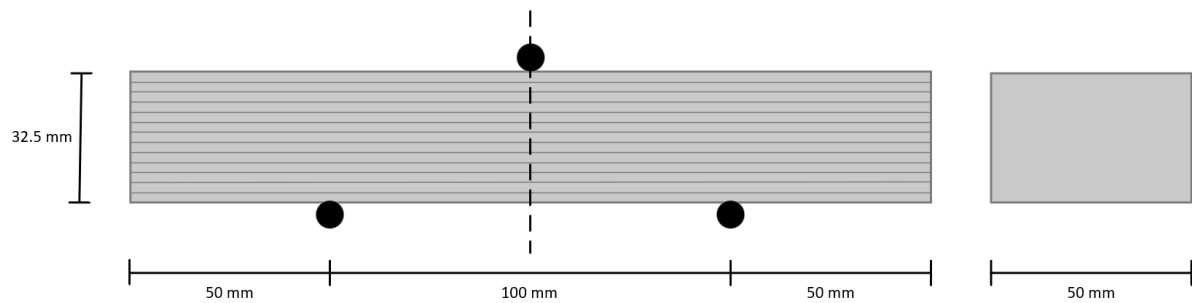


Figure 3.9: Visualisation of three-point bending test of 3D-printed specimen

4

Results

This chapter describes the results that are received from the several tests that are done within the research. Firstly, the results of the CT scan are given in section 4.1. Secondly, in section 4.2 a comparison of the results of the CT scanning with the model introduced in section 2.1 is done. Lastly, the results of the three-point bending test are discussed and analysed in section 4.3.

4.1. CT scan

After the specimens are scanned using the CT scanning machine, different analyses can be done. First, the air-void ratio is determined for each type of specimen. This is shown in Table 4.1 and Figure 4.1 where 'Ref' represents the cast reference specimen. This specimen is used to look at the influence of 3D-printing of concrete and compare it to conventionally cast concrete. Since one specimen of each type of specimen is scanned, it is possible that this value is not a good representation of all the specimens.

Table 4.1: Results of CT scan

Printing direction	Pore volume [mm ³]	Total cropped volume [mm ³]	Air-void ratio [%]
Ref	1,572.47	244,326.00	0.644
0°	2,324.92	182,749.64	1.272
45°	1,336.87	184,832.35	0.723
90°	2,312.80	180,212.50	1.283

The distribution in Figure 4.1 shows that all printed specimens have a (slightly) higher air-void ratio compared to the reference specimen. These extra air voids are introduced by the printing technique. When processing the data from the specimen, a cropped version of the specimen is used to exclude the outer parts, which may introduce additional imperfections.

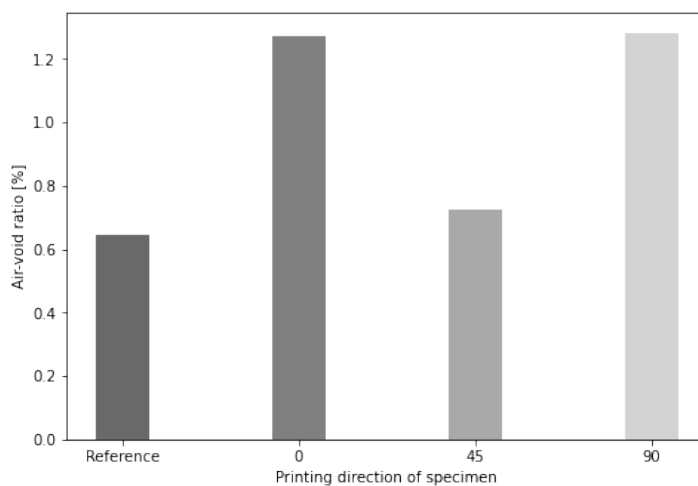


Figure 4.1: The air-void ratio of each type of specimen

The results of each type of specimen are described below.

4.1.1. 0° printed specimen

Figure 4.2 shows the pores with a volume of at least 1 mm³ in the 0° printed specimen. Figure 4.5 shows all pores within this specimen that are considered in this research having a volume of at least 0.004 mm³. The distribution of pores can be seen in the histogram in Figure 4.4. This specimen shows a relatively high number of large defects, seen in the yellow, red, and green linear air voids. This indicates a relatively poor printing quality. This means that a significant amount of discontinuities were present during printing.

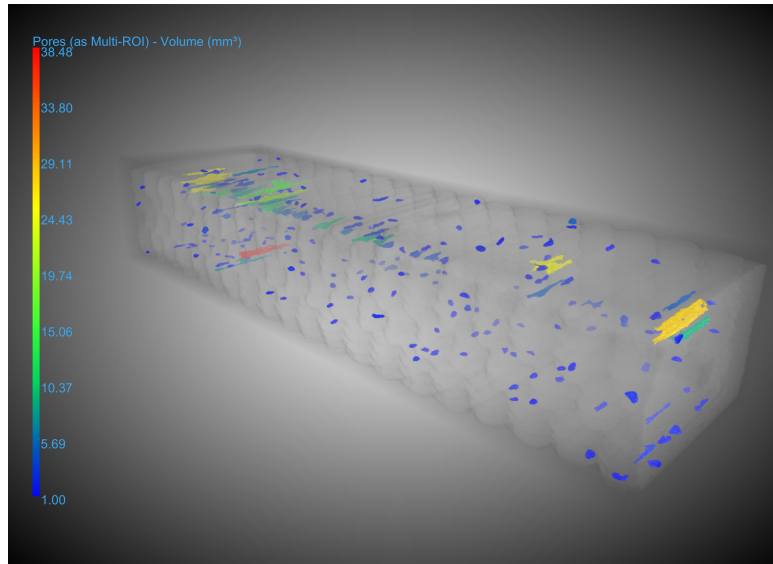


Figure 4.2: 3D visualisation of pores in 0° printed specimen

Figure 4.3 shows the vascular system of the 0° printed specimen. The vascular system shows some imperfections on the top side, indicating again poor printing quality. This figure shows what regions a healing agent can reach when applying a self-healing cycle.

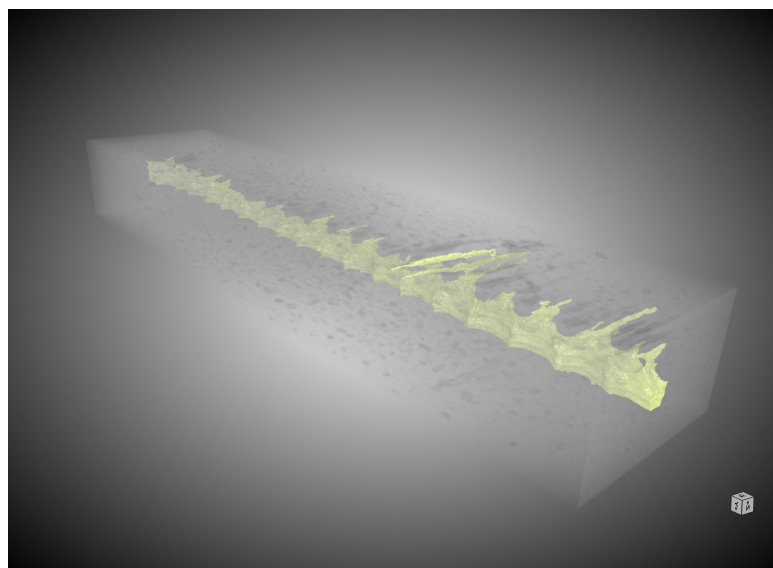


Figure 4.3: Visualisation of the vascular system of the 0° printed specimen

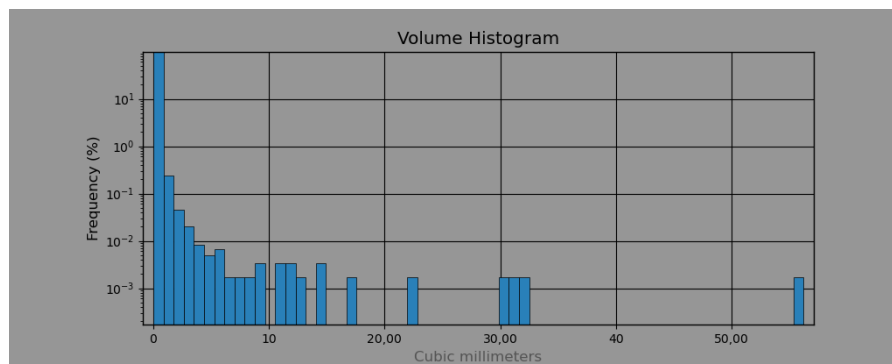


Figure 4.4: Logarithmic histogram of pore distribution of 0° specimen

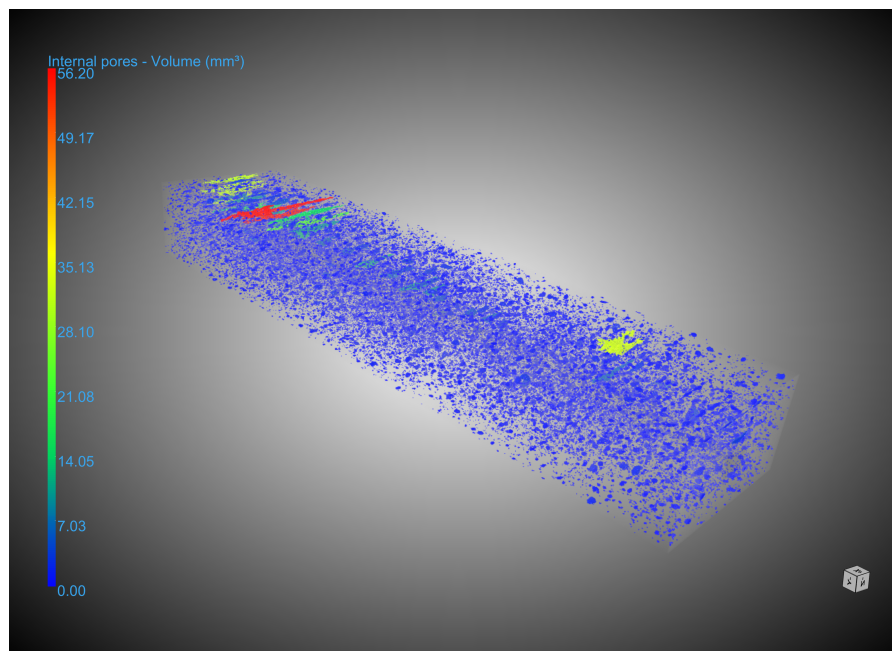


Figure 4.5: Visualisation of all pores in 0° specimen ($\text{volume} > 0.004 \text{ mm}^3$)

When looking at Figure 4.5 one might argue that the red pores on the top of the specimen are due to the cropping of the specimen in DragonFly. This is, however, not the case. This can be seen in Figure 4.6. When looking at the pore up close, it is present that the pore is within the cropped volume and is due to a printing error.

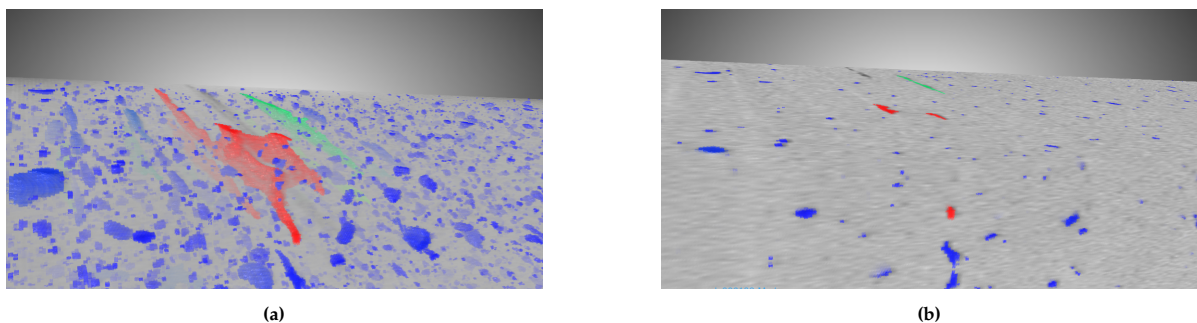


Figure 4.6: (a) Transparent view of big pore (b) Solid view of big pore

4.1.2. 45° printed specimen

Figure 4.7 shows the pores with a volume of at least 1 mm³ in the 45° printed specimen. Figure 4.10 shows all pores within this specimen that are considered in this research having a volume of at least 0.004 mm³. The distribution of pores can be seen in the histogram in Figure 4.9. This specimen shows almost no imperfections, indicating a high printing quality. This can also be due to the interlocking of the layers, forcing out excess air during the printing process.

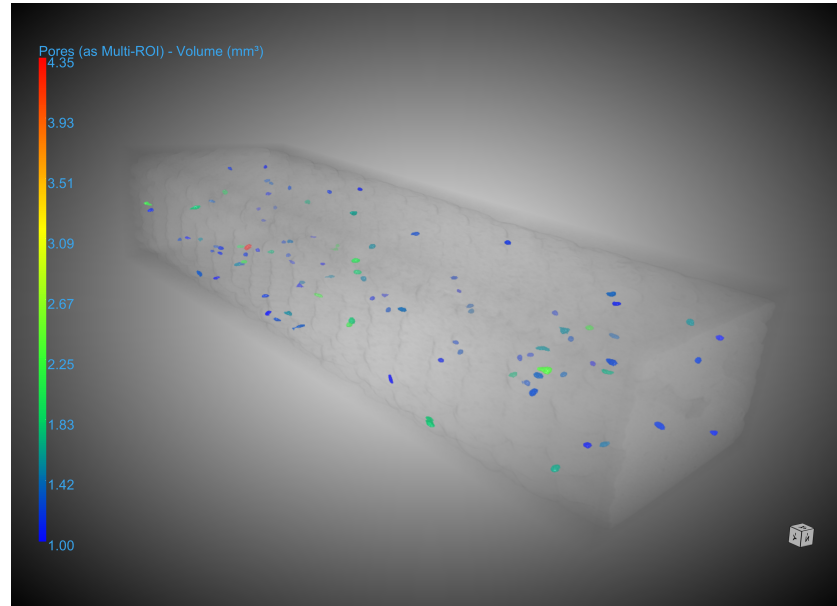


Figure 4.7: 3D visualisation of pores in 45° printed specimen

Figure 4.8 shows the vascular system of the 45° printed specimen. The vascular system shows almost no imperfections due to the printing process, indicating again a high printing quality. This figure shows what regions a healing agent can reach when applying a self-healing cycle.

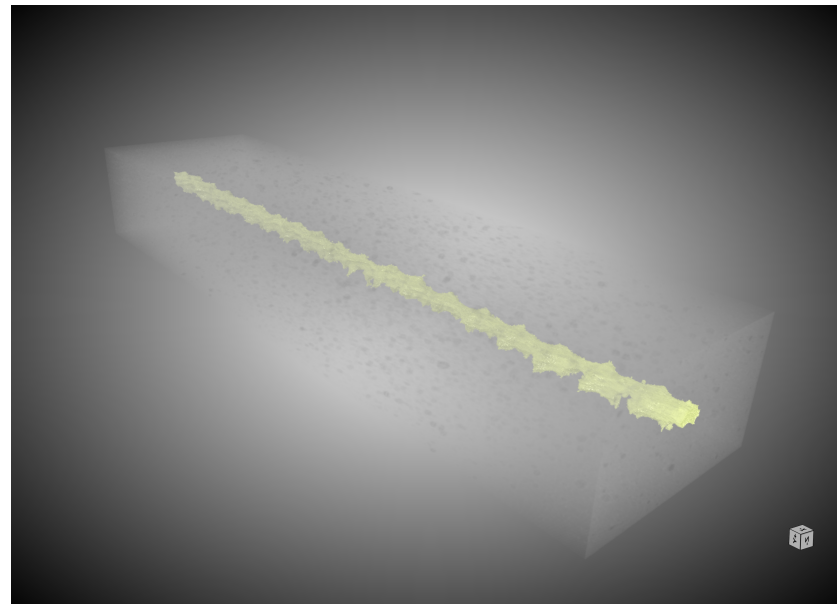


Figure 4.8: Visualisation of the vascular system of the 45° printed specimen

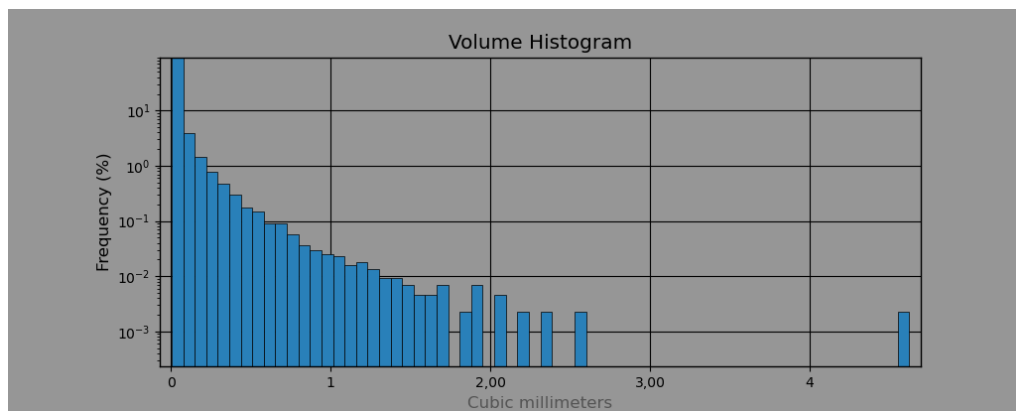


Figure 4.9: Logarithmic histogram of pore distribution of 45° specimen

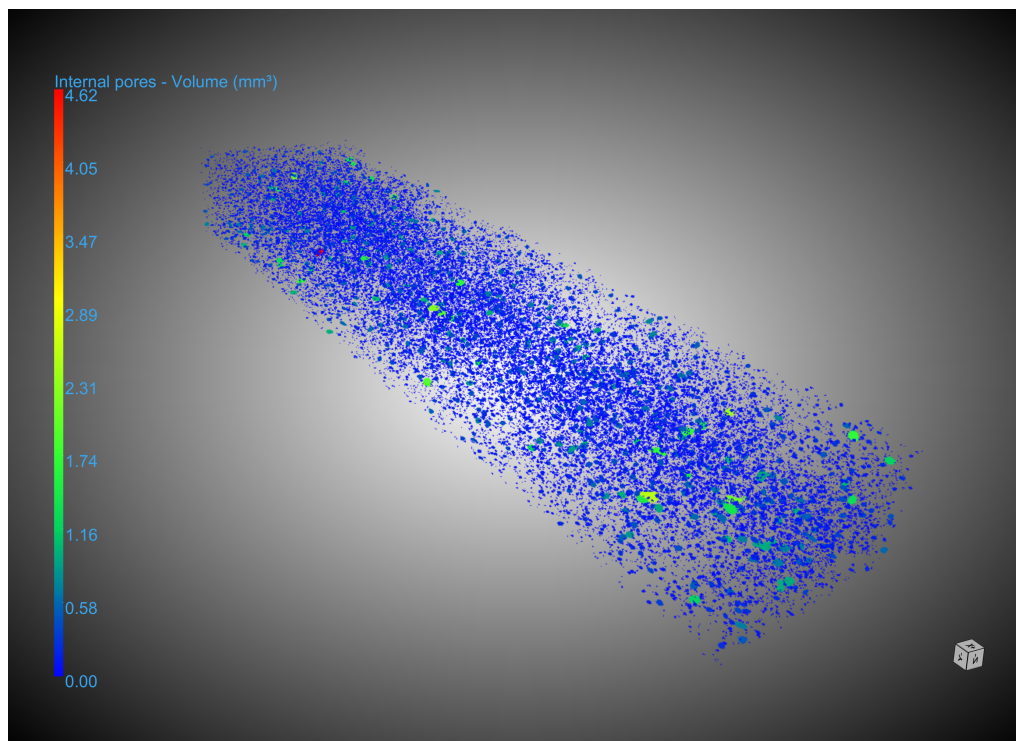


Figure 4.10: Visualisation of all pores in 45° specimen (volume > 0.004 mm³)

4.1.3. 90° printed specimen

Figure 4.11 shows the pores with a volume of at least 1 mm³ in the 90° printed specimen. Figure 4.14 shows all pores within this specimen that are considered in this research having a volume of at least 0.004 mm³. The distribution of pores can be seen in the histogram in Figure 4.13. This specimen shows some imperfections in red and yellow. These imperfections will be mainly due to the printing process, indicating an intermediate printing quality.

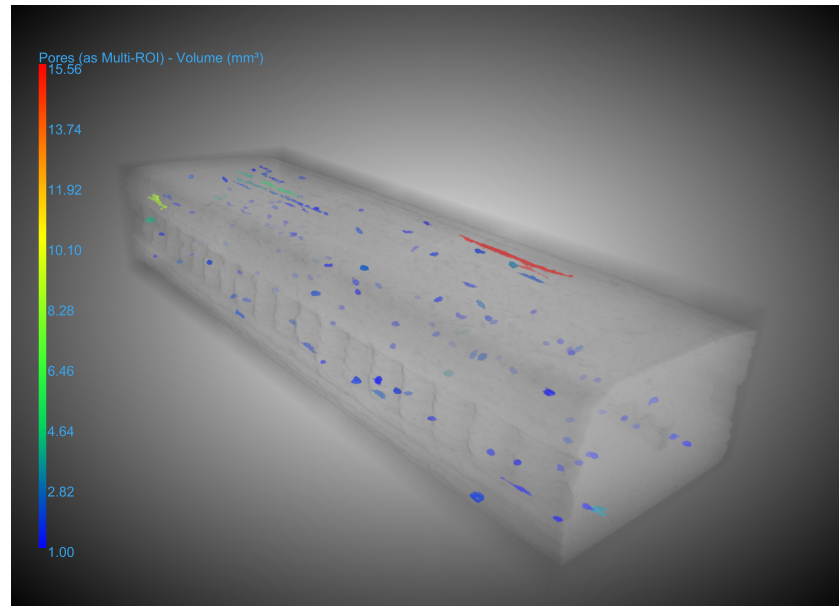


Figure 4.11: 3D visualisation of pores in 90° printed specimen

Figure 4.12 shows the vascular system of the 90° printed specimen. The vascular system shows almost no imperfections due to the printing process, indicating good printing quality. This figure shows what regions a healing agent can reach when applying a self-healing cycle.

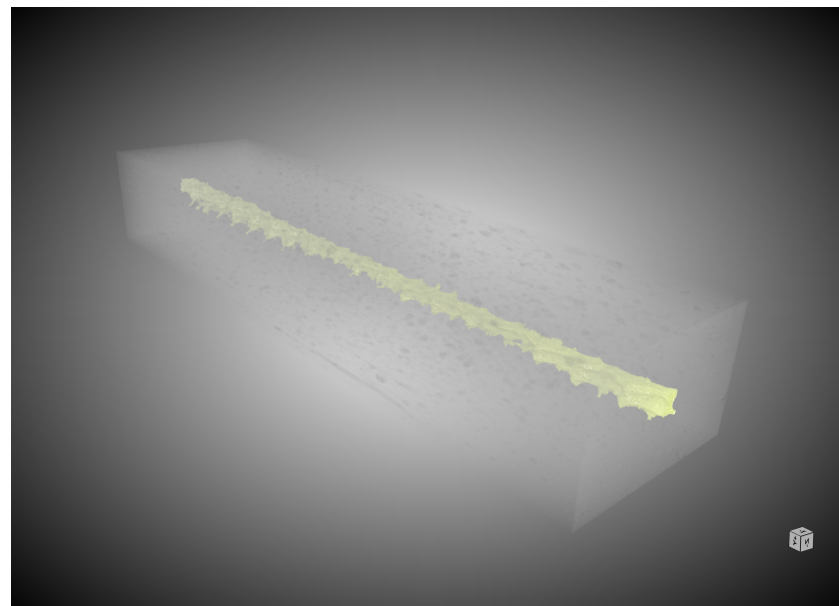


Figure 4.12: Visualisation of the vascular system of the 90° printed specimen

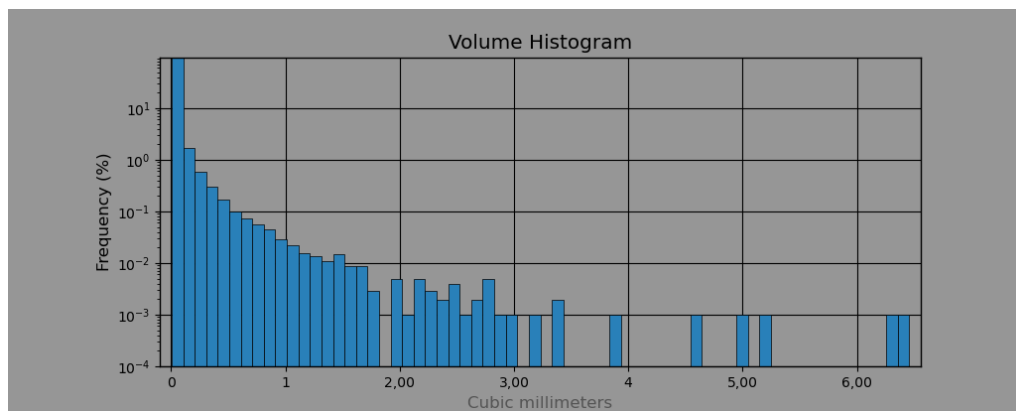


Figure 4.13: Logarithmic histogram of pore distribution of 90° specimen

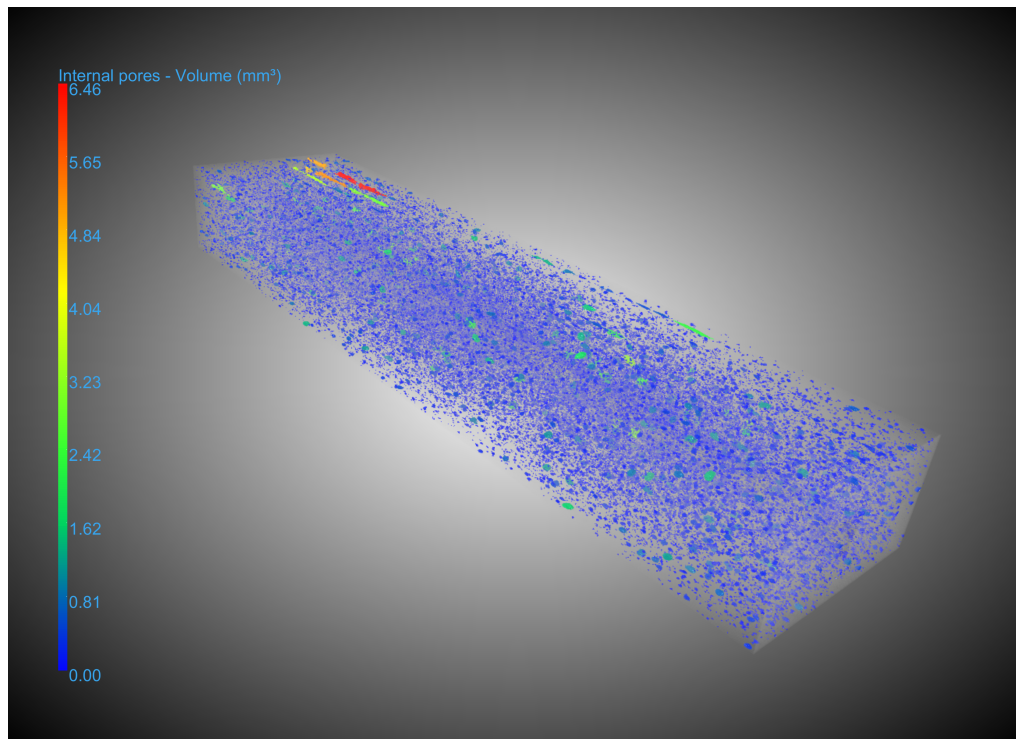


Figure 4.14: Visualisation of all pores in 90° specimen (volume > 0.004 mm³)

4.1.4. Reference specimen

Figure 4.15 shows the pores with a volume of at least 1 mm^3 in the reference specimen. Figure 4.17 shows all pores within this specimen that are considered in this research having a volume of at least 0.004 mm^3 . The distribution of pores can be seen in the histogram in Figure 4.16.

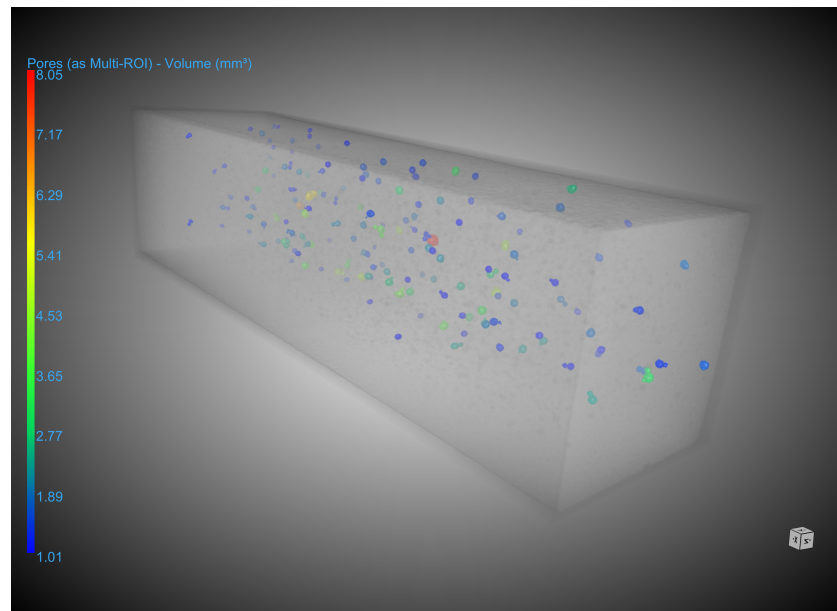


Figure 4.15: 3D visualisation of pores in reference specimen

From this figure, it is clear that the lower part of the reference specimen has fewer to no pores in comparison to the middle and top parts. This is mainly due to the casting process, which included vibration of the specimens. The top layers exert pressure on the pores during casting, forcing the pores to float upwards. The lower the pores, the more pressure is exerted and the higher the chance the pores float upwards.

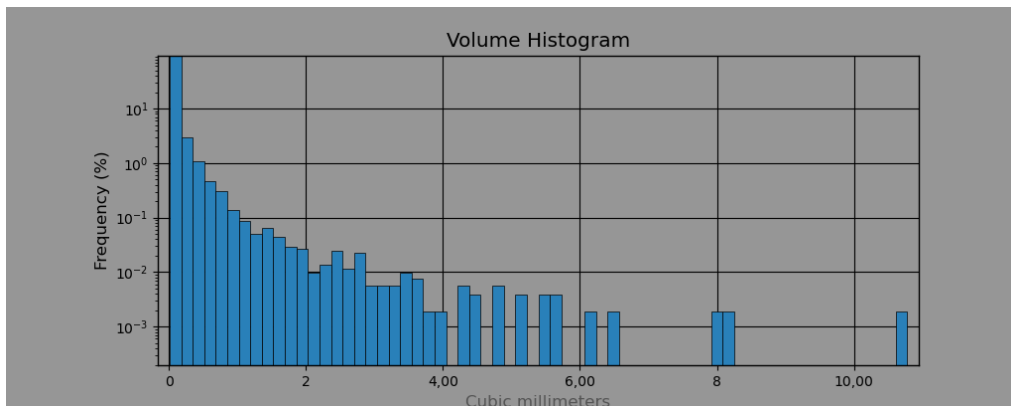


Figure 4.16: Logarithmic histogram of pore distribution of reference specimen

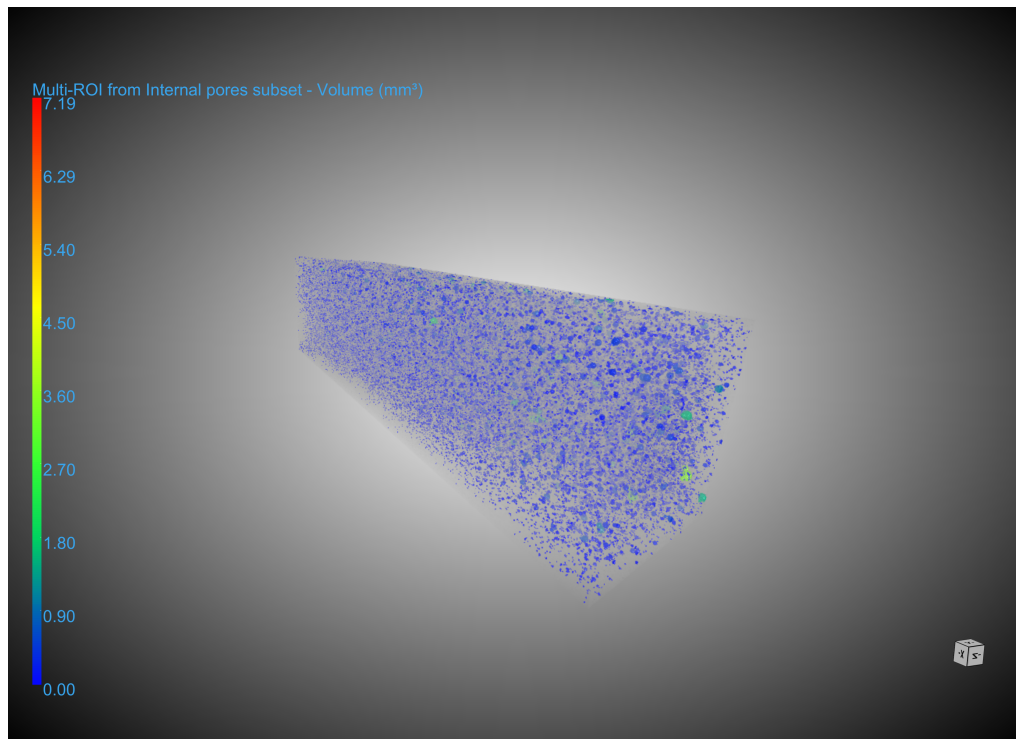


Figure 4.17: Visualisation of all pores in reference specimen (volume > 0.004 mm³)

4.1.5. Additional CT scanning results

Table 4.2 shows additional results from CT scanning. The table shows the total volume of the specimen, volume of the vascular, and length of the vascular.

Table 4.2: Additional results of CT scan

Printing direction	Total uncropped volume [mm ³]	V_{va} [mm ²]	l_{va} [mm]
Ref	246,812.71	-	-
0°	339,597.46	3,768.68	185.27
45°	348,625.24	1,825.94	185.32
90°	355,549.03	2,535.73	185.39

4.2. Comparing results to the air void model

The air void model introduced in section 2.1 can be used to estimate the air-void ratio of the 0° and 90° specimens. The model is not applicable for 45° specimens, since the mathematics behind this are not worked out. This section will reflect on the model's accuracy. The input for the model is retrieved from the CT scanning data and processed using DragonFly and Python. In this section, the vertical and horizontal distances between the concrete lines are measured and put into the model. The results can be seen in Figure 4.18. The model predicts an air-void ratio of 16.3% and 8.3% for the 0° and 90° specimens respectively.

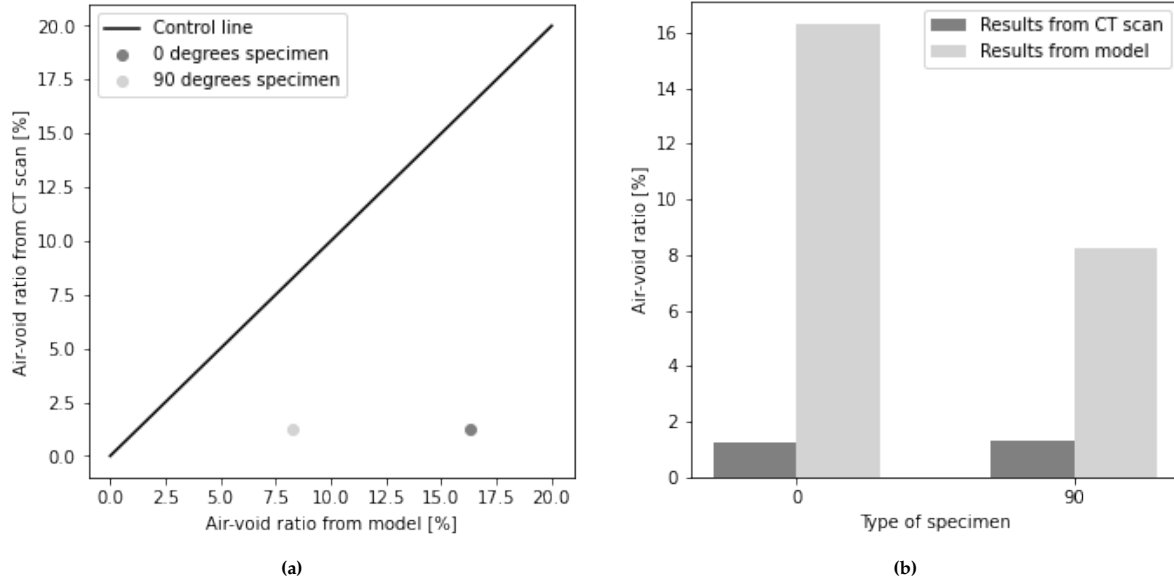


Figure 4.18: Comparing the results of the CT scanning with the results of the model with (a) a graph plot and (b) a bar plot

The input for the model is shown in Table 3.1 and Table 4.3. The distances need to be measured highly accurately because a slight change in value results in a significant change in the air-void ratio. There may be instances when the distance between the centres of a line varies throughout the specimen, in that case, an average needs to be taken.

Table 4.3: Input air void model

Printing direction	A_{va} [mm 2]	d_h [mm]	d_v [mm]
0°	152.60	5.14	2.76
90°	13.68	5.01	2.53

The model estimates a lower porosity for the 90° printed specimen in comparison to the 0° printed specimen. This indicates a higher strength for the 90° specimen relative to the 0° printed specimen.

4.3. Three-point bending test

All the specimens are tested as described in section 3.3. The results of the three-point bending test are shown below in Table 4.4. Three reference specimens were made, while two specimens of each printing direction were made.

Table 4.4: Three-point bending force

Printing direction	Specimen 1 [kN]	Specimen 2 [kN]	Specimen 3 [kN]	Mean [kN]
Ref	3.529	3.924	4.460	3.971
0°	2.875	1.801	-	2.338
45°	2.616	2.739	-	2.891
90°	2.813	2.739	-	2.776

A bar plot showing the mean three-point bending force of every type of specimen can be seen in Figure 4.19a. Figure 4.19b shows the relation between the air-void ratio of a specimen and the flexural strength. The trend line shows a clear negative relationship between the two properties, however, the number of data points is not sufficient to validate this. The trend line may be of a higher degree in reality, but due to the number of data points, a first-degree line is chosen. In reality, the trend line is likely shaped in the form of an inverse exponential function.

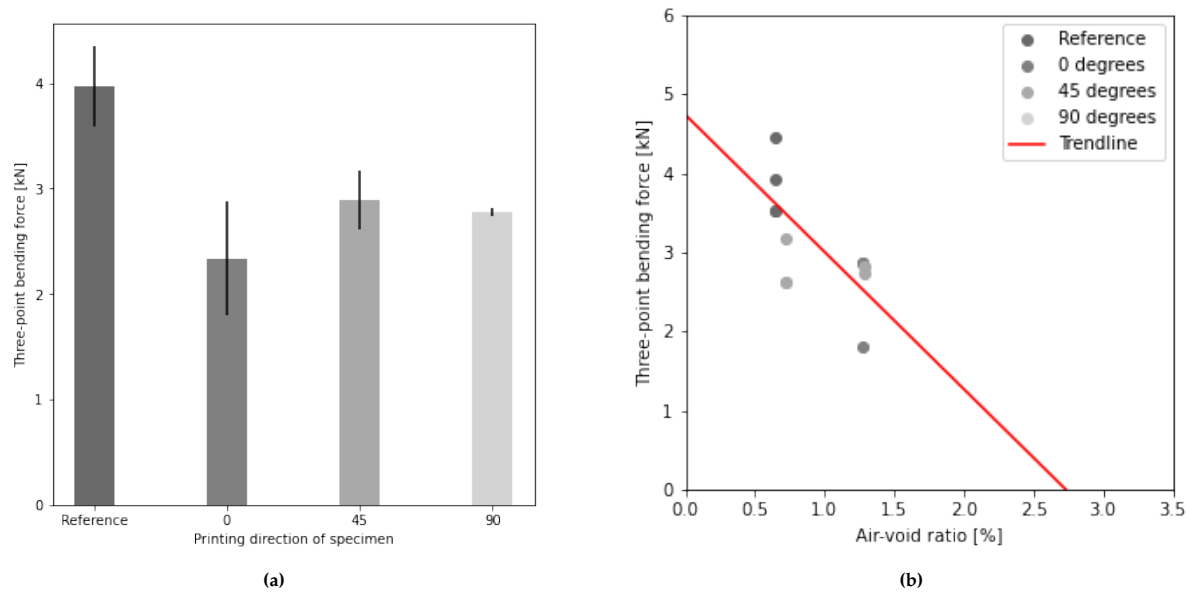


Figure 4.19: (a) A bar graph showing the mean three point bending force of each type of specimen; (b) A plot showing the relation between the air-void ratio and the three point bending force

The specimens were tested until a crack developed. The concrete specimens did not entirely fail because of the ductile behaviour, due to the fibres in the concrete mix. Images of the three-point bending test and cracked specimens can be found in Appendix C. The results show that the reference specimen can withstand the highest three-point bending force, and the 0° can withstand the lowest. The results also show that the 45° and 90° have similar strength.

It should be taken into account that the reference specimens have a completely different cross-section in comparison to the printed specimens. Although the cross-sectional areas of both types of specimens are quite similar, the printed specimens contain a vascular system and the reference specimens do not. While the reference specimens have a cross-sectional area of $(40 \cdot 40 =) 1600 \text{ mm}^2$, the printed specimens have a cross-sectional area of $(50 \cdot 32.5 - 7.5 \cdot 7.5 =) 1569 \text{ mm}^2$.

The flexural strength can be calculated from the data received by the three-point bending test and the geometry of the specimens. To do this, it is assumed that the cross-section of the specimens is constant, with a height of 32.5 mm and a width of 50 mm. It is furthermore assumed that the vascular is constant with a height and width of 7.5 mm. The flexural strength of each type of specimen can be seen in Figure 4.20 and Table 4.5.

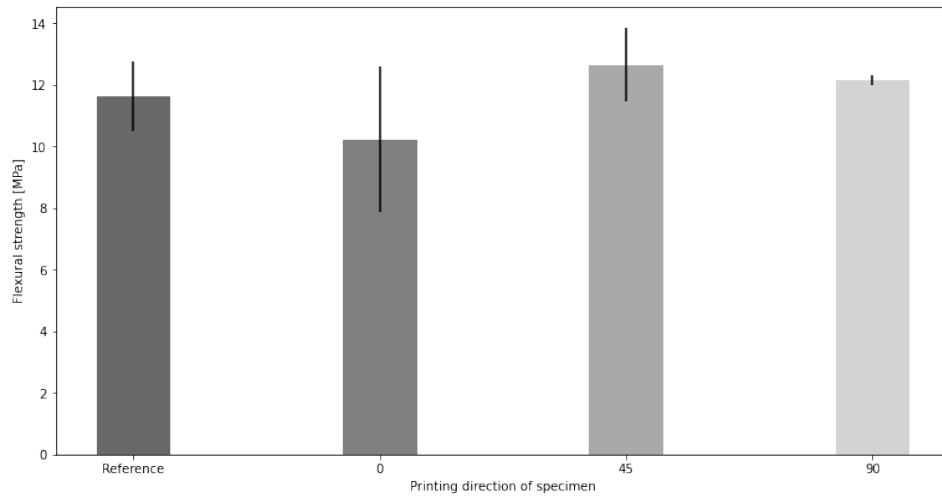


Figure 4.20: Flexural strength of every type of specimen

The results show that all the specimens have similar flexural strengths. The similarity can be explained by the fact that the same concrete mix was used for all the specimens. The slight differences can be explained by imperfections.

Table 4.5: Cracking stress of specimens

Printing direction	Ref	0°	45°	90°
Flexural strength [MPa]	11.634	10.235	12.654	12.152

5

Discussion

This research contained the testing of specimens to examine the influence of printing direction on flexural strength and porosity. Two specimens of each printing direction and three cast reference specimens are made to test and validate this influence.

The results show that the 45° printed specimens have the lowest porosity while having the highest flexural strength. This means that a lower amount of imperfections positively impacts the strength of the concrete. This may be due to the interlocking effect of the printing direction, improving the isotropy of the specimen. The reason behind the relatively high porosity of the 0° and 90° printed specimens is likely the printing quality. The poor printing quality of the specimen introduced large imperfections which created large voids, increasing the air-void ratio. New specimens have to be made to test and validate the porosity of the design of the concrete specimen.

The model predicts higher porosities in comparison to the result of the CT scanning. This can be explained by errors present in the model and/or errors during the analysing process. Because of the resolution, only pores with a minimum volume of 0.004 mm³ are considered, while pores with a lower volume are considered as noise. Leaving out these pores significantly changes the air-void ratio. This can be mitigated by using a higher resolution during CT scanning. The model has a couple of assumptions, these assumptions may also be the cause of the differences.

6

Conclusions

This report aims to investigate the influence of the printing direction on the porosity and flexural strength of 3D-printed vascular self-healing concrete. This is done to contribute to a better understanding of 3D-printed concrete for the construction industry. To test this, a total of nine specimens are made and tested.

It appeared, from research, that the 45° printing direction had the lowest porosity with 0.72%. While the 0° and 90° possessed similar porosity of about 1.28%. This difference is due to the printing technique. It shows that having the same direction layers on top of each other introduces significantly more imperfection (air voids).

A model is constructed to estimate the porosity of 3D-printed concrete. The model shows differences with the real porosity. The air void model predicts a porosity of 16.3% and 8.3% for the 0° and 90° printed specimens respectively, while the real air-void ratios were 1.27% and 1.28% respectively. This shows that some errors exist within the air-void model or within the analysing process.

When testing the flexural strength of the different specimens, it becomes clear that the reference specimen can withstand a higher three-point bending force in comparison to the printed specimens. The data of every type of specimen can be seen in Table 6.1.

Table 6.1: Data of each type of specimen

Printing direction	Ref	0°	45°	90°
Porosity [%]	0.644	1.272	0.723	1.283
Porosity according to model [%]	-	16.305	-	8.256
Three-point bending force [kN]	3.971	2.338	2.891	2.776
Flexural strength [MPa]	11.634	10.235	12.654	12.152

The results show a negative relation between the air-void ratio and flexural strength, which is in line with research done by Lian et al. (2011). The results also show that the 45° printing direction has the lowest porosity and the highest flexural strength of the printed specimens. This clearly indicates that the 45° printing direction is the most efficient design.

Because of the relatively low amount of specimens, it is not with certainty that the 45° printed specimen is the strongest. Because of the relatively short research time, too few specimens are made to test and validate the strength.

7

Recommendations

This research is bound by a time restriction, meaning that only a certain amount of specimens could be made. Scientific research requires as many specimens as possible to rule out any imperfections or outliers. Because of the relatively short research time, too few specimens were printed to check and validate the air void model or analyse the correlation between printing direction and flexural strength. This research gives a first impression of the properties of each printing direction, but more specimens have to be tested to validate this.

Future research could focus on improving the model in several ways. The model can be improved by taking into account the printing quality (e.g., the number of imperfections), the exact shape of the concrete lines, and the sagging of the concrete during printing. These factors have not yet been taken into account due to complexity and lack of time. Taking these factors into account can be done by making more specimens of different printing parameters and testing them. Now it is assumed that the concrete lines have an elliptical shape which is constant during printing, but this can differ depending on the printing quality. The model can also be improved by adjusting it for the 45° printed specimens, which can be done mathematically.

Apart from the model, the specimens themselves can also be researched further. For example, by making hybrid specimens with each layer having a different printing direction to increase the isotropy of the specimen. The first and last four layers of the specimens were printed in the same direction, but having different printing directions between these four layers may also positively influence the strength and healing efficiency of the specimen.

Lastly, a four-point bending test can be executed to test and validate the flexural strength of the specimens. Measuring the strength with more types of tests gives a better representation of the real strength.

References

- Cabrera, J. (1996). Deterioration of concrete due to reinforcement steel corrosion. *Cement and Concrete Composites*, 18(1), 47–59. [https://doi.org/10.1016/0958-9465\(95\)00043-7](https://doi.org/10.1016/0958-9465(95)00043-7)
- Hughes, G. B., & Chraibi, M. (2012). Calculating ellipse overlap areas. *Computing and Visualization in Science*, 15(6), 291–301. <https://doi.org/10.1007/s00791-013-0214-3>
- Li, Z., de Souza, L. R., Litina, C., Markaki, A. E., & Al-Tabbaa, A. (2020). A novel biomimetic design of a 3d vascular structure for self-healing in cementitious materials using murray's law. *Materials & Design*, 190, 108572. <https://doi.org/10.1016/j.matdes.2020.108572>
- Lian, C., Zhuge, Y., & Beecham, S. (2011). The relationship between porosity and strength for porous concrete. *Construction and Building Materials*, 25(11), 4294–4298. <https://doi.org/10.1016/j.conbuildmat.2011.05.005>
- Linke, R. (2017). Additive manufacturing, explained. *MIT Sloan*. Retrieved May 18, 2023, from <https://mitsloan.mit.edu/ideas-made-to-matter/additive-manufacturing-explained>
- Matest. (2023). *Cement-mortar*. Retrieved June 15, 2023, from <https://www.matest.com/en/product/e161-01n-compression-and-flexural-machine-dual-range-250-15-kn-servo-plus-evolution>
- TESCAN. (2023). *Tescan coretom micro ct*. Retrieved May 16, 2023, from <https://info.tescan.com/coretom-micro-ct>
- Wan, Z., Xu, Y., Zhang, Y., He, S., & Šavija, B. (2022). Mechanical properties and healing efficiency of 3d-printed abs vascular based self-healing cementitious composite: Experiments and modelling. *Engineering Fracture Mechanics*, 267, 108471. <https://doi.org/10.1016/j.engfracmech.2022.108471>

A

Background air void model

The model explained in section 2.1 is mathematically determined based on the ellipsoidal shape of the concrete lines of the 3D printer. The background of the model is given below.

Enclosed area

Two equations that describe an ellipse are used. Firstly, the following equation describes the function of an ellipse with the origin in the middle of the ellipse (Hughes and Chraibi, 2012):

$$\frac{x^2}{a^2} + \frac{y^2}{b^2} = 1 \quad (\text{A.1})$$

Secondly, the following equation can be used to determine the area of an ellipse:

$$A = \pi \cdot a \cdot b \quad (\text{A.2})$$

Using these formulas, the total width of a cross-section can be determined. This is done using the number of lines in the vertical direction (n_v) and horizontal direction (n_h). Solving Equation A.1 for x and y gives the following two equations:

$$x = \sqrt{a^2 - \frac{y^2 \cdot a^2}{b^2}} \quad (\text{A.3})$$

$$y = \sqrt{b^2 - \frac{x^2 \cdot b^2}{a^2}} \quad (\text{A.4})$$

With a the semi-minor axis and b the semi-major axis. These parameters both depend on the width and height of a concrete line. a is equal to $\frac{b_l}{2}$ and b is equal to $\frac{h_l}{2}$, with b_l the width of a concrete line and h_l the height of a concrete line. Substituting this in Equation A.3 and Equation A.4 gives:

$$x = \sqrt{\frac{b_l^2}{4} - \frac{y^2 \cdot b_l^2}{h_l^2}} \quad (\text{A.5})$$

$$y = \sqrt{\frac{h_l^2}{4} - \frac{x^2 \cdot h_l^2}{b_l^2}} \quad (\text{A.6})$$

With these equations, the height and width of bonding concrete lines can be found. The vertical bonding equals $w_{b,v}$ and the horizontal bonding equals $w_{b,h}$. An ellipse that bonds another ellipse at the left or right side results in a reduction of the width of the ellipse. This reduction in width can be calculated by calculating the x-value of the bond by setting the y-value as $0.5 \cdot w_{b,v}$, see Figure A.1.

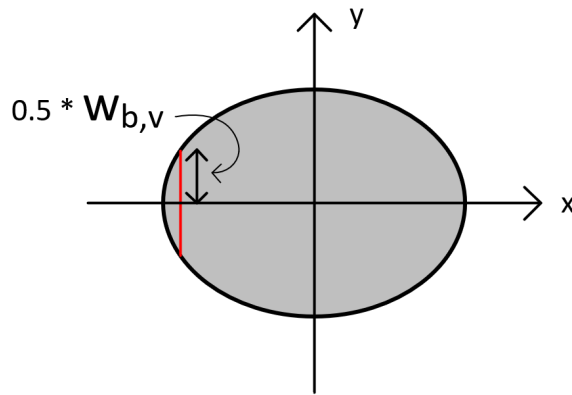


Figure A.1: Determining the width of a side-bonded concrete line

Substituting $y = 0.5 \cdot w_{b,v}$ into Equation A.5 gives the following equation. Please note that the value is given as a positive value, this is done because the value is a distance:

$$x = \sqrt{\frac{b_l^2}{4} - \frac{w_{b,v}^2 \cdot b_l^2}{4 \cdot h_l^2}} \quad (\text{A.7})$$

When looking at Figure 2.1 it can be determined that this width is present $n_h \cdot 2 - 2$ times in the width of the specimen. But to get the total width, b_l needs to be added because of the edge lines which are not bonded on one side. The total width becomes:

$$b_t = \sqrt{\frac{b_l^2}{4} - \frac{w_{b,v}^2 \cdot b_l^2}{4 \cdot h_l^2}} \cdot (2n_h - 2) + b_l \quad (\text{A.8})$$

To determine the height of a top and/or bottom bonded line, the previous steps need to be repeated, but now looking at the y-direction. Figure A.2 shows the principle of this. To determine the y-value of the bonding $x = 0.5 \cdot w_{b,h}$ needs to be substituted into Equation A.6.

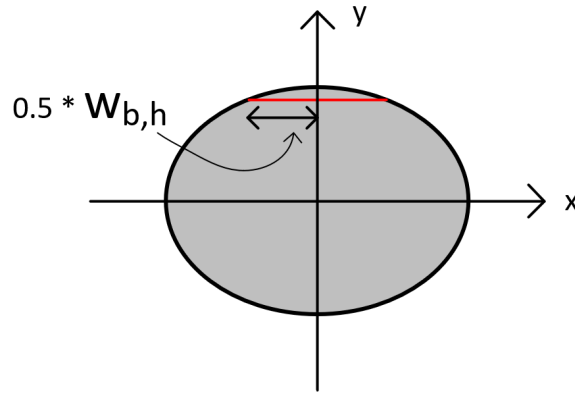


Figure A.2: Determining the height of a top-bonded concrete line

The substitution results in the following equation:

$$y = \sqrt{\frac{h_l^2}{4} - \frac{w_{b,h}^2 \cdot h_l^2}{4 \cdot b_l^2}} \quad (\text{A.9})$$

When looking at Figure 2.1 it can be determined that this height is present $n_v \cdot 2 - 2$ times in the height of the specimen. But to get the total height h_l needs to be added because of the top and bottom lines which are not bonded on one side. The total height becomes:

$$h_t = \sqrt{\frac{h_l^2}{4} - \frac{w_{b,h}^2 \cdot h_l^2}{4 \cdot b_l^2}} \cdot (2n_v - 2) + h_l \quad (\text{A.10})$$

To determine the total enclosed area, Equation A.8 needs to be multiplied with Equation A.10 which results in:

$$A_0 = b_t \cdot h_t = \left(\sqrt{\frac{b_l^2}{4} - \frac{w_{b,v}^2 \cdot b_l^2}{4 \cdot h_l^2}} \cdot (2n_h - 2) + b_l \right) \cdot \left(\sqrt{\frac{h_l^2}{4} - \frac{w_{b,h}^2 \cdot h_l^2}{4 \cdot b_l^2}} \cdot (2n_v - 2) + h_l \right) \quad (\text{A.11})$$

Concrete area

To determine the concrete area, Equation A.2 is used. This equation calculates the area of one concrete line, to determine the total concrete area this value needs to be multiplied by the total number of concrete lines. This results in the following equation:

$$A_c = n_v \cdot n_h \cdot \pi \cdot \frac{b_l}{2} \cdot \frac{h_l}{2} = n_v \cdot n_h \cdot \frac{1}{4}\pi \cdot b_l \cdot h_l \quad (\text{A.12})$$

Vascular system

The presence of the vascular system needs to be considered in the model. This is done by subtracting the area of the vascular system from the equation. This area of the vascular system is A_{va} . The area of the vascular system is not constant throughout the cross-section, an average needs to be taken. The area of the system depends on the printing direction because the model looks at a cross-section perpendicular to the printing direction. When looking at a 0° printed specimen A_{va} can be calculated by using Equation A.13.

$$A_{va,0} = \frac{h_{va} \cdot l_{va} \cdot b_{va}}{b_t} \quad (\text{A.13})$$

The vascular system is not present in every cross-section, by using this equation the system is spread over the width of the specimen, making every cross-section the same.

When looking at a 90° printed specimen, the area can be calculated by multiplying the height of the system by the width. With this kind of specimen, every cross-section is the same, so the area of the vascular system can be calculated by the following formula:

$$A_{va,90} = h_{va} \cdot b_{va} \quad (\text{A.14})$$

Air-void ratio

To determine the air-void ratio, the total area of the voids needs to be divided by the total area of the concrete. This is done in the following equation:

$$r_v = \frac{A_0 - A_{va} - A_c}{A_0 - A_{va}} = 1 - \frac{n_v \cdot n_h \cdot \frac{1}{4}\pi \cdot b_l \cdot h_l}{b_t \cdot h_t - A_{va}} \quad (\text{A.15})$$

This model can be used for either 0° or 90° printed concrete. One may argue that the material to the left of the red line in Figure A.1 and above the red line in Figure A.2 is now not taken into consideration. This is, however, not true. The area of the concrete is still the same, only this material is now not in this position but is used to further bond with the neighbouring concrete line. This needs to be taken into consideration when determining the vertical and horizontal bonding widths.

B

Images of specimens

0° printing direction



Figure B.1: Front view of 0° specimen being printed

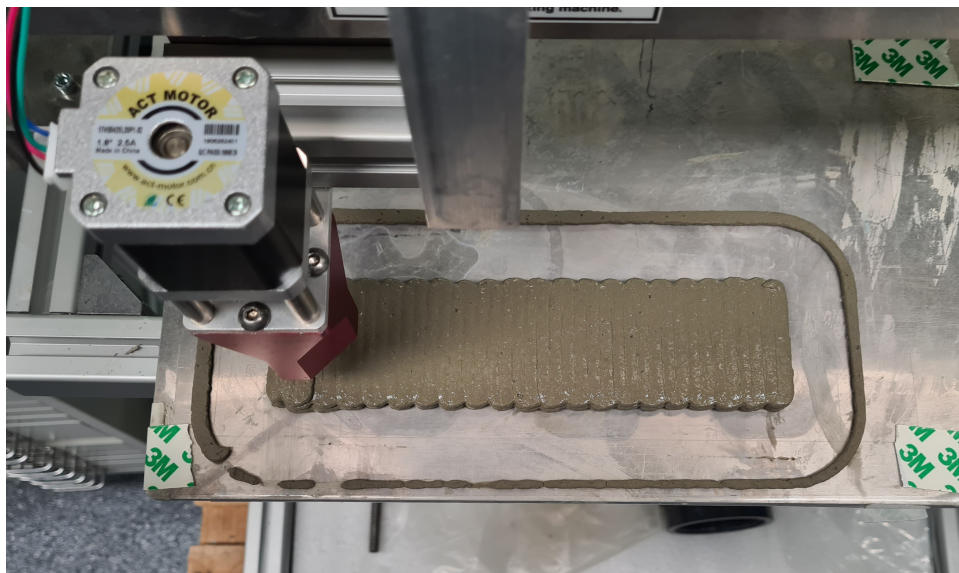


Figure B.2: Top view of 0° specimen being printed

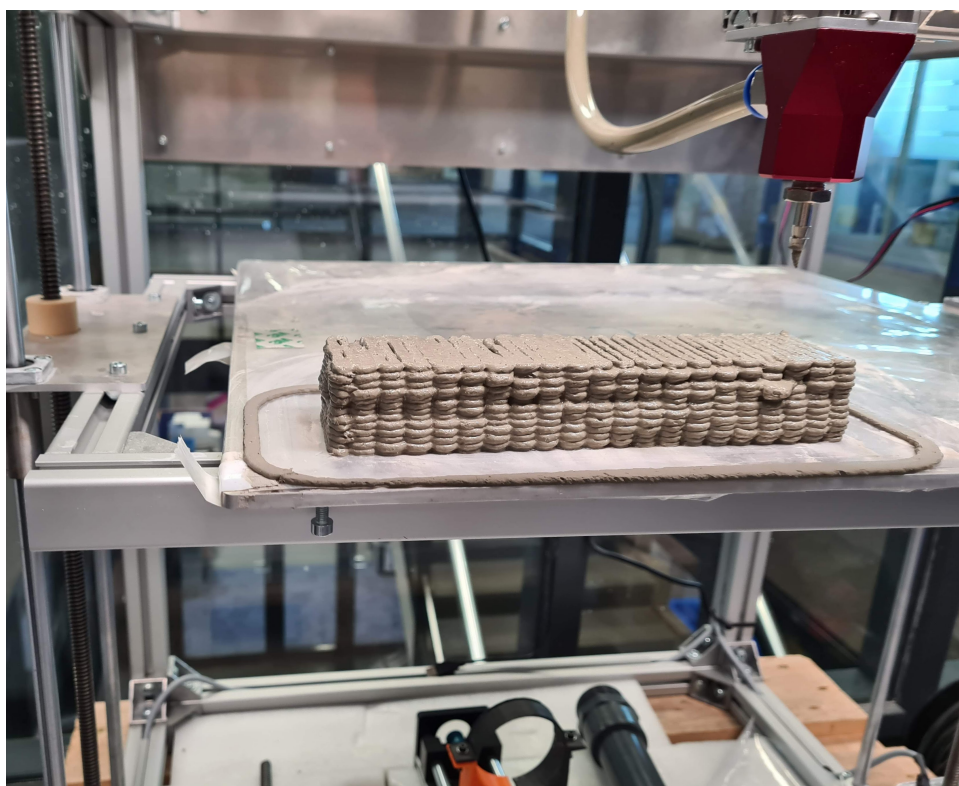


Figure B.3: Image of finished 0° printed specimen

45° printing direction

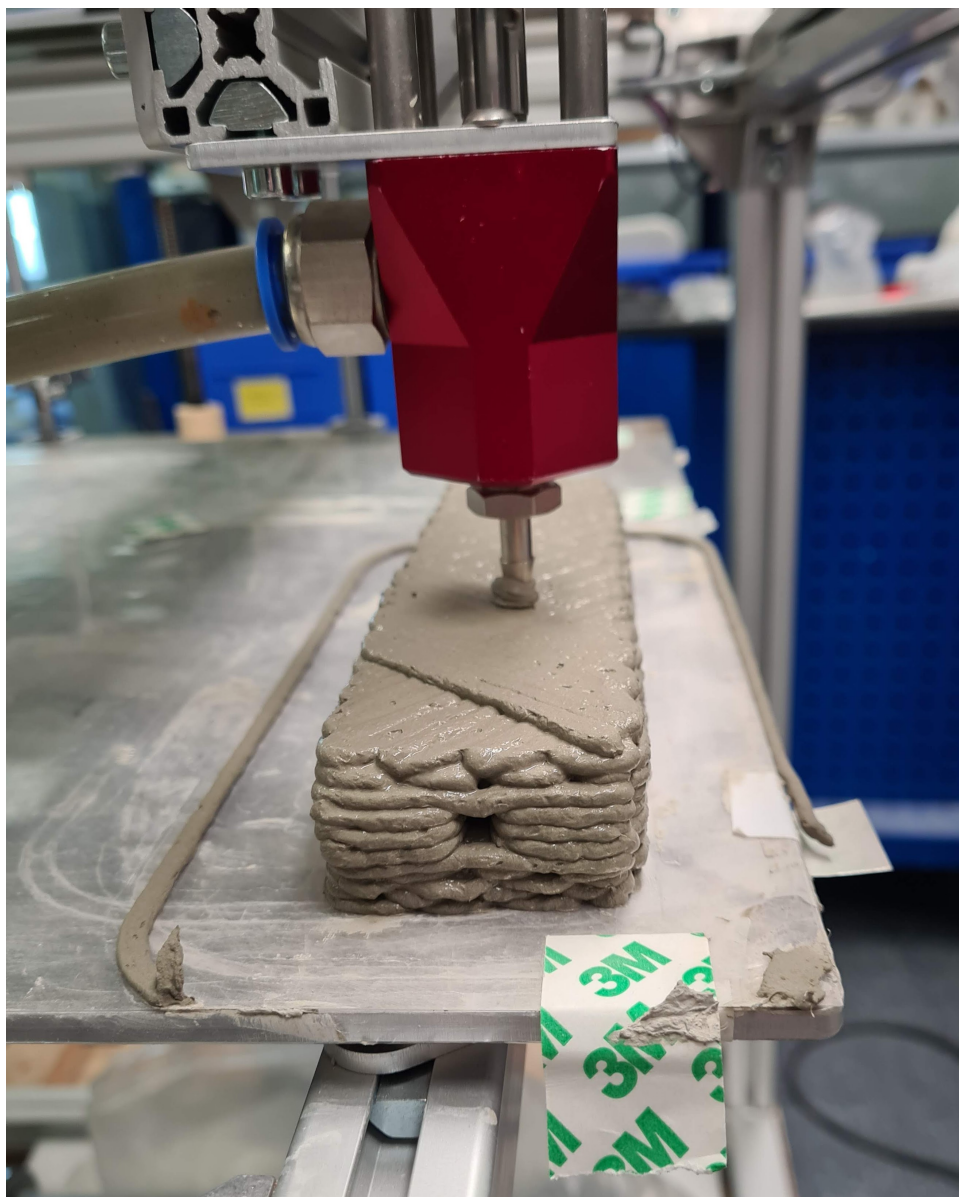


Figure B.4: Front view of 45° specimen almost finished



Figure B.5: Front view of vascular system being printed

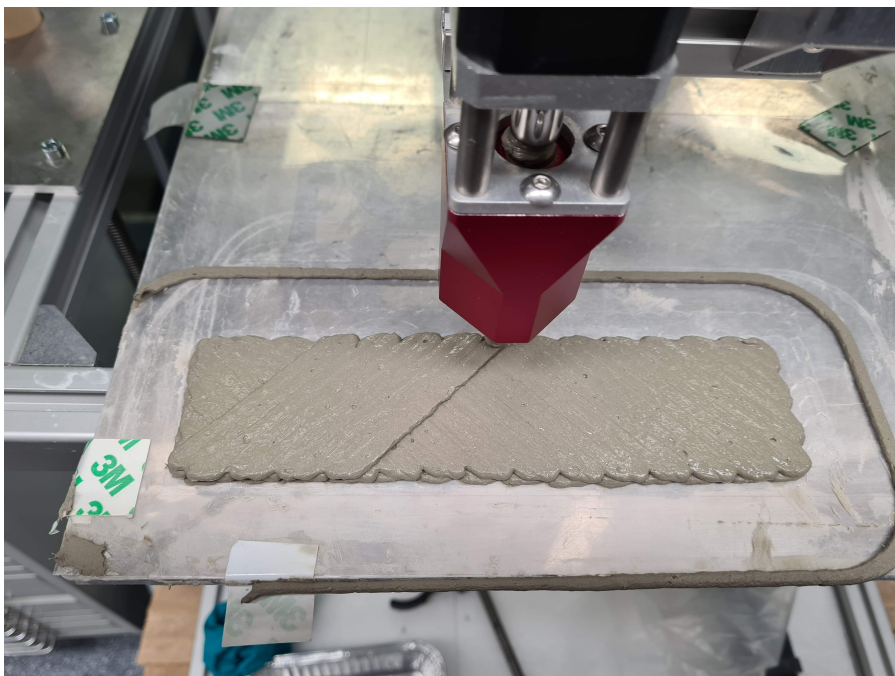


Figure B.6: Top view of 45° specimen being printed

90° printing direction



Figure B.7: front view of 90° specimen being printed

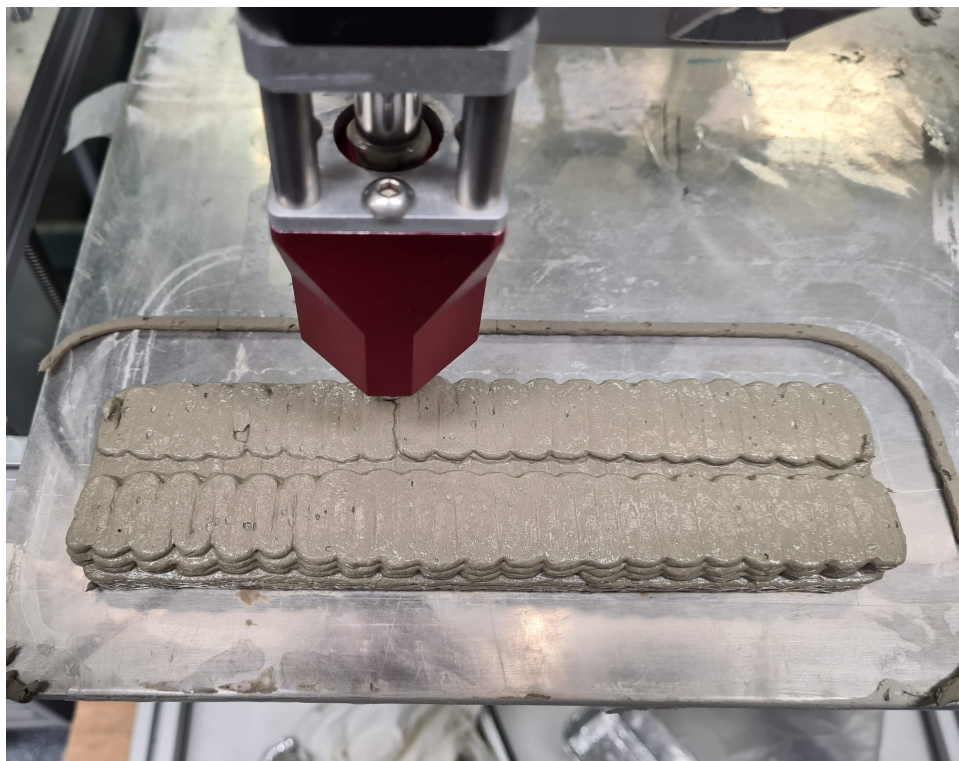


Figure B.8: Top view of 90° specimen being printed



Figure B.9: Front view of finished 90° specimen

C

Images of three-point bending test and cracked specimens

Images of three-point bending test



(a)



(b)

Figure C.1: (a) Front view of three-point bending test; (b) Back view of three-point bending test

Images of crack development of specimens

0° cracks



Figure C.2: Top view of both cracks in the 0° specimens



Figure C.3: Side view of crack in the first 0° specimen



Figure C.4: Side view of crack in the second 0° specimen

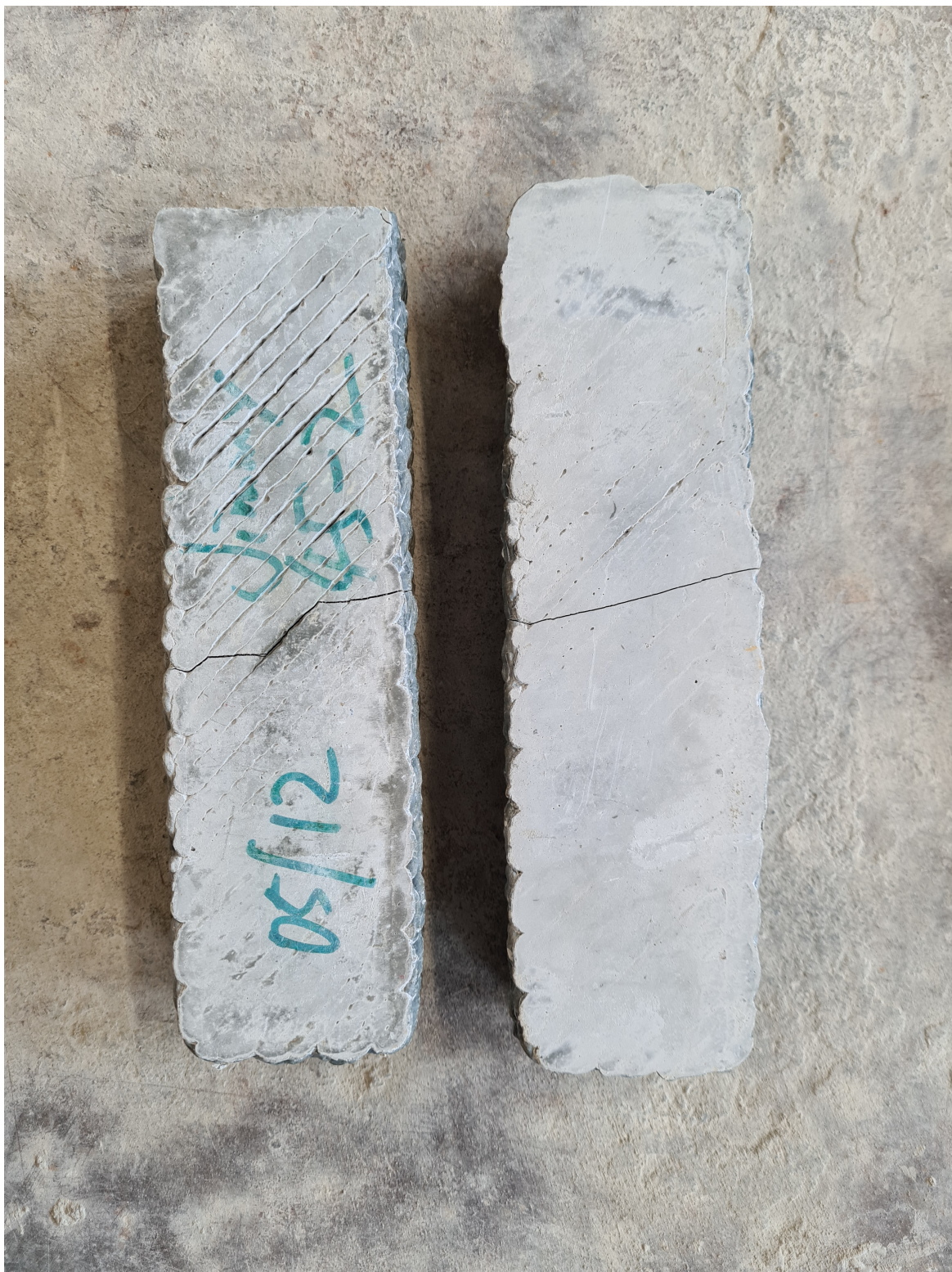
45° cracks

Figure C.5: Top view of both cracks in the 45° specimens



Figure C.6: Side view of crack in the first 45° specimen



Figure C.7: Side view of crack in the second 45° specimen

90° cracks

Figure C.8: Top view of both cracks in the 90° specimens



Figure C.9: Side view of crack in the first 90° specimen



Figure C.10: Side view of crack in the second 90° specimen

Reference cracks



Figure C.11: Top view of both cracks in the reference specimens



Figure C.12: Side view of crack in the first Reference specimen



Figure C.13: Side view of crack in the second Reference specimen



Figure C.14: Side view of crack in the third Reference specimen